

國立臺灣大學 物理學研究所

碩士論文

氮化鋁鎵／氮化鎵異質結構的電性傳輸

**Electrical transport in AlGa_N/Ga_N
heterostructures**

指導教授：梁啓德、張本秀

研究生：吳坤達

中華民國九十四年七月

To my parents

誌謝

能完成這本論文，實在不是我一個人的力量。首先感謝梁啓德老師在學術研究上不斷督促與叮嚀，讓我在碩士生涯體驗到做實驗的樂趣。還有張顏暉老師與陳永芳老師也給予我在學術研究上許多建議與關懷，讓我做實驗時能更順利。

此外，我還要感謝石明峰同學。無論什麼時候，在我做實驗需要幫忙時，他總能伸出援手幫忙我完成許多實驗上的種種困難。還有在做實驗時，不斷提醒我容易出錯的地方，讓我能順利完成每項量測工作。在此特別感謝石明峰同學在我碩士生涯給予我很大的幫助。

再來是長庚大學連少棠同學。本論文所使用的樣品都是由連少棠同學長出來的。我則負責量測工作。而他所長的樣品有很高的重覆性，樣品的接腳也呈現良好的歐姆特性，使量測工作輕鬆許多。還有平常有許多實驗上的問題，也跟連少棠同學一起討論受益良多。

事實上這是我第一次寫長篇英文論文。因此有很多句子表達方法或修辭用得不恰當。特別感謝陳繼偉同學、宋明瑾學妹和趙妍絜學妹給予我英文寫作上的幫忙與建議。

最後，要謝謝我的父母給予我精神上的支持與肯定，使我在學術研究上能無後顧之憂，全力以赴。謹將本論文獻給所有關心我的人。

摘要

在本論文中，我將描敘氮化鋁鎵／氮化鎵高電子遷移率電晶體的兩項研究。論文總共分爲兩大部份。

1. 氮化鋁鎵／氮化鎵高電子遷移率電晶體在不同鋁成份下傳輸特性

我們探討三塊不同鋁成份的氮化鋁鎵／氮化鎵高電子遷移率電晶體的傳輸性質。鋁的成份分別爲 1 1 %、1 5 % 和 2 5 %。這三塊樣品都成長在藍寶石基板上，而遷移率的量測顯示 1 5 % 鋁成份的氮化鋁鎵／氮化鎵高電子遷移率電晶體有最高的遷移率。其遷移率在溫度 1 0 K 時，爲 $6\,600\text{ cm}^2/\text{V s}$ 。如果鋁的成份大過 1 5 %，那樣品的遷移率將大幅下降。

此外，我們發現三塊樣品的遷移率在室溫下幾乎一樣。這是因爲在溫室下，聲子散射主宰電子的全部散射，而由樣品雜質所產生的散射相較之下微不足道。

再者，我們發現二維電子濃度隨著在氮化鋁鎵中鋁成份的增加而增加。我們也對二維電子濃度做定量計算也發現同樣的趨勢。這個理由是因爲當鋁成份增加，在氮化鋁鎵中的極化也增加。而這個增加的極化現象，在氮化鋁鎵和氮化鎵的界面產生更多片電荷形成。因此，更多電子將被吸引到這裡來補償在氮化鋁鎵／氮化鎵界面附近的

片電荷。所以對於一個有較高鋁成份的氮化鋁鎵／氮化鎵的樣品，其二維電子濃度也會比較高。

我們同時測量氮化鋁鎵／氮化鎵高電子遷移率電晶體的活化能，而發現活化能隨著鋁成份增加而增加。當鋁成份增加，在氮化鋁鎵和氮化鎵之間的晶格不匹配愈來愈大。而這個增加的晶格不匹配將導致較大的缺陷密度。因此需要更高的活化能來熱激發載子到二維電子系統中。

總而言之，我們研究結果顯示出 15% 鋁成份的氮化鋁鎵／氮化鎵高電子遷移率電晶體有最高的遷移率。而這個事實告訴我們可以用 15% 鋁成份來成長其它氮化鋁鎵／氮化鎵高電子遷移率電晶體，以獲得最高的遷移率。

2. 成長在正型矽基板上關於氮化鋁鎵／氮化鎵高電子遷移率電晶體的測量

在前一章節所使用的基板是藍寶石。然而，藍寶石在工業上並沒有矽來得普遍。因此，我們企圖在矽基板上成長我們的樣品。然而，在矽基板上成長高品質的氮化鎵是有困難的，因為在矽與氮化鎵之間有約 17% 的晶格不匹配和約 54% 的熱膨脹係數不匹配的缺點。

在本章節中，我們在樣品中分別沈積 5 秒和 10 秒的氮化矽薄

膜來增加氮化鎵的品質，而再和沒有沈積氮化矽薄膜的樣品做比較來觀察這樣一個薄膜如何影響在氮化鋁鎵和氮化鎵界面處的二維電子遷移率。在溫度 10 K 時，沒有沈積氮化矽薄膜的樣品，其遷移率為 $744 \text{ cm}^2/\text{Vs}$ 。相反地，有沈積 5 秒和 10 秒氮化矽薄膜的樣品，其遷移率分別為 $2333 \text{ cm}^2/\text{Vs}$ 和 $2387 \text{ cm}^2/\text{Vs}$ 。這結果顯示出在樣品中沈積氮化矽薄膜後，樣品的遷移率大幅提升三倍之多。

再來把這章的研究結果和上一章比較，我們發現在藍寶石基板上，鋁成份 15% 的氮化鋁鎵／氮化鎵有較高的遷移率。其遷移率為 $6600 \text{ cm}^2/\text{Vs}$ 。因此我們可以推斷出，在矽基板上成長氮化鋁鎵／氮化鎵高電子遷移率電晶體，其遷移率要和藍寶石上成長的一樣高是有困難的。然後，樣品遷移率大帳提昇的這項事實展示了我們在樣品裡沈積氮化矽薄膜這項技術的實用性。如果我們對成長樣品的技術做更進一步的研究，比如成長溫度，樣品結構，還有最重要的沈積氮化矽的技術，也許在矽基板上成長的高電子遷移率電晶體可以在傳統藍寶石上成長的一樣好。

Abstract

In this thesis, I will report on two measurements on AlGa_xN/GaN high electron mobility transistors (HEMTs). This thesis consists of the following two parts.

1. Transport in Al_xGa_{1-x}N/GaN HEMTs with different Al compositions

We performed measurements on three Al_xGa_{1-x}N/GaN HEMTs with different Al contents (11%, 15%, and 25% respectively). All three samples are grown on sapphire substrates, and the mobility measurements indicate that Al_xGa_{1-x}N/GaN HEMTs with 15% Al content have the highest mobility (6600 cm²/Vs at 10 K). If the Al content of Al_xGa_{1-x}N/GaN HEMTs exceeds 15%, the mobility will drop drastically.

In addition, we found that the mobilities of the three samples are almost identical at room temperature. This is because electron-phonon scattering dominates the electrical scattering at room temperature, and the electron-imperfection scattering due to impurities in the sample is small compared with electron-phonon scattering.

Furthermore, we found that the 2DEG concentration increases with increasing Al content in Al_xGa_{1-x}N. Quantitative calculation of the 2DEG concentration was performed and the same trend was obtained. The reason for this is that when the Al fraction increases, the polarization in Al_xGa_{1-x}N increases and induces more sheet charges at the interface of Al_xGa_{1-x}N and GaN. Therefore, for an Al_xGa_{1-x}N/GaN heterostructure with a higher Al composition, more electrons would be attracted to compensate for the sheet charges near the Al_xGa_{1-x}N/GaN interface. Hence the 2DEG concentration would be higher for an Al_xGa_{1-x}N/GaN sample with a higher Al composition.

We also measured the activation energy of Al_xGa_{1-x}N/GaN HEMTs, and found that the activation energy increases with increasing Al content. As the Al content increases, the lattice mismatch between Al_xGa_{1-x}N and GaN becomes more prominent. This increased lattice mismatch could induce a larger defect density. Therefore a higher activation energy is

required to thermally activate the carriers into the 2DEG region.

Finally, the fact that $\text{Al}_x\text{Ga}_{1-x}\text{N}/\text{GaN}$ HEMTs with 15% Al content has the highest mobility suggests that we can grow other AlGaN/GaN HEMTs with 15% Al content for the greatest mobility.

2. Measurements of AlGaN/GaN HEMTs grown on p-type

silicon substrates

The substrate used in the previous section is sapphire. However, sapphire is not as popular as Si in the industry. We therefore attempt to grow our samples on Si substrates. However, growing high-quality GaN on silicon substrates proves difficult because of the large lattice mismatch (about 17%) and large thermal mismatch (about 54%) between Si and GaN.

In this section, we inserted a thin Si_5N_4 film with deposition time of 5 seconds and 10 seconds to improve the GaN quality, and observed how such a thin film could affect the 2DEG mobility at the interface of AlGaN and GaN in comparison with the case without a Si_5N_4 thin film. At 10 K, the sample without the Si_5N_4 thin film had mobility $744 \text{ cm}^2/\text{Vs}$, whereas for the samples with 5 seconds and 10 seconds deposition time of Si_5N_4 it was $2323 \text{ cm}^2/\text{Vs}$ and $2387 \text{ cm}^2/\text{Vs}$ respectively. The result showed that the mobility was greatly enhanced by as much as three times after the Si_5N_4 thin film was inserted.

Upon comparing the mobility with the results of the previous chapter, we see that $\text{Al}_{0.15}\text{Ga}_{0.85}\text{N}/\text{GaN}$ HEMTs on sapphire substrates had a much higher mobility of $6600 \text{ cm}^2/\text{Vs}$. We conclude that it is difficult to grow AlGaN/GaN HEMTs on silicon substrates with mobilities as high as those grown on sapphire substrates. Nevertheless, this great enhancement of the mobility demonstrates the usefulness of our technique. If we perform further investigations on the optimization of our growth temperature, HEMT structure, and most importantly, Si_5N_4 treatment technique, it is expected that the quality of HEMTs grown on Si substrates may well be as high as those grown on conventional sapphire substrates.

Contents

Chapter 1

Introduction.....	1
1-1 Introduction.....	1
1-2 Density of states.....	2
1-3 AlGaN/GaN electron system.....	6
1-4 Ohmic contact.....	7

Chapter 2

Theoretical Background.....	10
2-1 Hall effect.....	10
2-1-1 Introduction.....	10
2-1-2 Theoretical derivation for 3-dimension.....	10
2-1-3 Two-dimensional Hall effect.....	14
2-1-4 Experimental techniques.....	14
2-2 Classical Drude model.....	16
2-3 Van der Pauw measurement.....	18
2-3-1 Introduction.....	18
2-3-2 Theoretical derivation.....	20
2-3-3 Contact displacement errors.....	22
2-3-4 Practical application.....	24

Chapter 3

Experimental Instruments.....	27
3-1 Close cycle system.....	27
3-1-1 Introduction.....	27
3-1-2 Close cycle device.....	27
3-1-3 Experimental steps.....	28
3-2 Hall effect system.....	30
3-2-1 Introduction.....	30

3-2-2 Hall measurement device.....	30
3-2-3 Experimental steps.....	32

Chapter 4

Transport in $\text{Al}_x\text{Ga}_{1-x}\text{N}/\text{GaN}$ HEMTs with different Al

compositions.....34

4-1 Introduction.....	34
4-2 Experiment.....	36
4-3 Results and discussions.....	38
4-4 Summary.....	47

Chapter 5

Measurements of $\text{AlGaIn}/\text{GaIn}$ HEMTs grown on p-type

silicon substrates.....51

5-1 Introduction.....	51
5-2 Experiment.....	52
5-3 Results and discussions.....	54
5-4 Summary.....	58

Chapter 6

Conclusions.....61

Lists of Figures

Chapter 1

Introduction

<i>Figure 1-1</i>	1
<i>A heterostructure of two materials with different band gaps.</i>	
<i>Figure 1-2</i>	3
<i>An electron is confined in 1-D box.</i>	
<i>Figure 1-3</i>	3
<i>Schematic diagrams of the density of states in 1-D system.</i>	
<i>Figure 1-4</i>	4
<i>An electron is confined in 2-D box.</i>	
<i>Figure 1-5</i>	4
<i>Schematic diagrams of the density of states in 2-D system.</i>	
<i>Figure 1-6</i>	5
<i>An electron is confined in 3-D box.</i>	
<i>Figure 1-7</i>	5
<i>Schematic diagrams of the density of states in 3-D system.</i>	
<i>Figure 1-8</i>	6
<i>Variation of the energy dependence for the density of states in (a) one-dimensional, (b) two-dimensional, and (c) three-dimensional system.</i>	
<i>Figure 1-9</i>	7
<i>The polarization distribution of AlGaN and GaN.</i>	

Chapter 2

Theoretical Background

<i>Figure 2-1</i>	12
<i>Schematic of the instrument set-up for the classical Hall effect.</i>	
<i>Figure 2-2</i>	13
<i>(a) When the electron passes through the sample, it will experience a magnetic Lorentz force, and will then tend to move downwards so as to accumulate at the bottom of the sample. (b) The electrons will continue to accumulate until they produce an electric field equal and opposite to the magnetic field acting on the remaining electrons. (c) If the carriers are holes, they will bend in the same direction just as the electrons do, but when we measure the side voltage, the sign of Hall potential will be reversed.</i>	
<i>Figure 2-3</i>	15
<i>A draft of a real four-points measurement case.</i>	
<i>Figure 2-4</i>	16
<i>A case of GaAs Hall measurement where the depth is 350 μm. By linear fitting of R_{xy} with respect to B, $R_{xy} = -0.03656 + 0.00168 B$, $R^2 = 0.9997$ where the slope is $0.00168 = \frac{1}{d e n}$. By substituting the depth of GaAs and electric charge into the equation, we can obtain the carrier density $n = 1.06 \times 10^{19} \text{ cm}^{-3}$.</i>	
<i>Figure 2-5</i>	19
<i>The classical idea for measuring the resistivity of a sample.</i>	
<i>Figure 2-6</i>	20
<i>Four-point measurements for a sample of any shape.</i>	
<i>Figure 2-7</i>	21
<i>Consider a sample with the shape of a semi-infinite plane.</i>	

Figure 2-8.....23
Assuming that our sample is circular in shape, we calculate the contact displacement errors when the diameter of the circle is D and the contact C' is a distanced d to the left of its original position.

Figure 2-9.....24
Before assuming that our sample is circular, we first assume our sample to be a semi-infinite plane. We subsequently transform our result to the circular problem.

Figure 2-10.....25
 $f(x) = e^{-ax} + e^{-bx} - 1$, where $a=1$ and $b=2$.

Chapter 3

Experimental Instruments

Figure 3-1.....28
The diagram of a close-cycle system.

Figure 3-2.....31
The eight modes of Hall measurement.

Figure 3-3.....31
The diagram of Hall effect system.

Chapter 4

Transport in $Al_xGa_{1-x}N/GaN$ HEMTs with different Al compositions

Figure 4-1.....36
The schematic diagram of $Al_xGa_{1-x}N/GaN$ heterostructure where x is 0.11, 0.15, and 0.25 respectively.

<i>Figure 4-2</i>	37
<i>The resistance as a function of temperature measured in the close cycle system. The result implies that the two-dimensional electron gas behaves like a metal.</i>	
<i>Figure 4-3</i>	38
<i>Resistivity as a function of temperature. This result strongly suggests that two-dimensional electron gas behaves like a metal.</i>	
<i>Figure 4-4</i>	39
<i>Two-dimensional carrier concentration as a function of temperature. We can see that the carrier concentration will increase with the increasing Al fraction in $Al_xGa_{1-x}N$.</i>	
<i>Figure 4-5</i>	42
<i>Carrier concentration as a function of Al composition. The solid line represents the theoretical calculation, and the spots represent the experimental measurements at 10 K.</i>	
<i>Figure 4-6</i>	43
<i>Mobility as a function of temperature.</i>	
<i>Figure 4-7</i>	44
<i>Mobility as a function of $1/T$. We can clearly see the linear dependence at room temperature.</i>	
<i>Figure 4-8</i>	45
<i>2DEG mobility at 10 K as a function of Al composition.</i>	
<i>Figure 4-9</i>	46
<i>Sample A: The logarithm of carrier concentration with respect to 1000 times the reciprocal of temperature. The activation energy is measured to be 10.8 meV.</i>	
<i>Figure 4-10</i>	46
<i>Sample B: The logarithm of carrier concentration with respect to 1000 times the reciprocal of temperature. The activation energy is measured to be 23.7 meV.</i>	

Figure 4-11.....47
Sample C: The logarithm of carrier concentration with respect to 1000 times the reciprocal of temperature. The activation energy is measured to be 25.9 meV.

Chapter 5

Measurements of AlGa_xN/GaN HEMTs on p-type silicon substrates

Figure 5-1.....53
The schematic diagram of Al_{0.15}Ga_{0.85}N/GaN heterostructure, where x is 0, 5, 10 respectively.

Figure 5-2.....54
The resistance as a function of temperature measured in the close cycle system. The result implies that the two-dimensional electron gas behaves like a metal.

Figure 5-3.....55
Resistivity as a function of temperature. We can see that the resistivity of samples with Si₃N₄ thin film was greatly reduced.

Figure 5-4.....56
The carrier concentration as a function of temperature.

Figure 5-5.....57
Mobility as a function of temperature. We can see that the mobility was greatly enhanced by about three times after we deposited a Si₃N₄ thin film in the sample.

Figure 5-6.....58
Mobility as a function of 1/T. We can see the linear dependence at room temperature.

Chapter 1

Introduction

1-1 Two-dimensional system

In most materials, electrons move in three dimensions without any restriction. In metals, electrons can move freely. However, in some special cases, electrons are forbidden from moving in one particular dimension, and are instead restricted to moving in the other two dimensions. In such cases, the electrons behave like a two-dimensional system. In Nature, there exist several two-dimensional systems, graphite being a very good example. When one measures the resistance of a piece of graphite, one will find that the resistance parallel to the sheet of graphite is much smaller than that perpendicular to the sheet. The explanation is that two-dimensional system behaves like a metal and there are

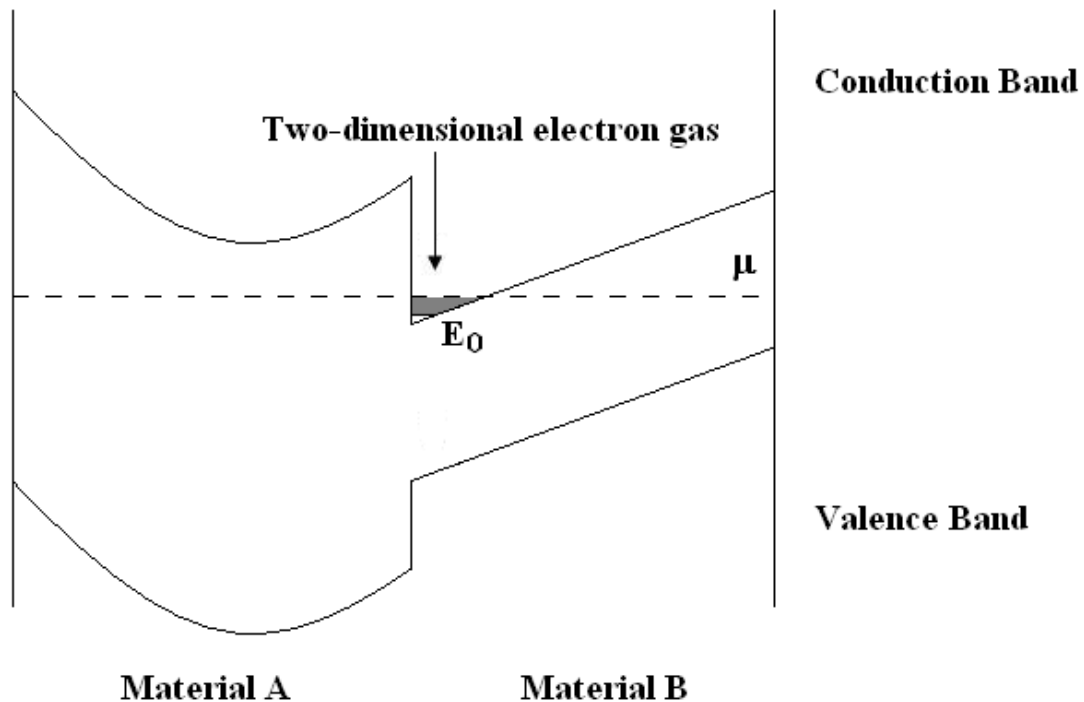


Figure 1-1. A heterostructure of two materials with different band gaps.

two-dimensional electrons in the graphite parallel to the sheet. These electrons dominate the transport along the direction parallel to the sheet, resulting in a much smaller resistance.

In semiconductors, we can also produce a two-dimensional system by changing the surface potential of the semiconductor so as to produce a triangular potential well as shown in figure 1-1. Electrons in the semiconductor could fall into this well and be confined in it, forming a two-dimensional electron system.

Recently, the techniques of growing sample have been improved tremendously. One can now use metal organic chemical vapor deposition (MOCVD) or molecular beam epitaxy (MBE) to grow atoms layer by layer, and we can easily produce a triangular potential well at the interface of two materials with different band-gaps.

1-2 Density of states

When studying solid-state physics, it is important to understand the concept of the density of states of a particular system, which will depend on the dimensions of the system. In this section, we will calculate the density of states in one-, two-, and three-dimensional systems, and compare the differences between these three cases.

By definition, the density of states is the number of electron states per unit volume per unit energy, and is often denoted by $N(E)$. As shown in figure 1-2, we consider an electron confined in a one-dimensional box. According to the Schrödinger equation, the energy level of the electron is given by

$$E = \frac{\hbar^2 \pi^2}{2 m L^2} n^2, \quad (1-1)$$

where n is a positive integer. Rewriting Eq. 1-1, we have

$$n = \frac{\sqrt{2 m E}}{\hbar \pi} L. \quad (1-2)$$

Taking the derivative on both sides, we obtain

$$dn = \frac{\sqrt{m}}{\sqrt{2} \pi \hbar} \frac{L}{\sqrt{E}} dE. \quad (1-3)$$

In a one-dimensional system as shown in figure 1-3,

$$N(E) = 2 \times \frac{dn}{L dE} = \frac{\sqrt{2m}}{\pi \hbar} \frac{1}{\sqrt{E}}. \quad (1-4)$$

Hence we have derived the one-dimensional density of states. The factor 2 is due to the electron spin degeneracy.

Similarly, we can derive the two-dimensional density of states by considering an electron confined in a two-dimensional box as shown in figure 1-4, Eq. 1-1 could be rewritten as

$$E = \frac{\hbar^2 \pi^2}{2mL^2} (n_x^2 + n_y^2) \equiv \frac{\hbar^2 \pi^2}{2mL^2} n^2, \quad (1-5)$$

where n_x and n_y are positive integers. Similarly, in a two-dimensional system as shown in figure 1-5

$$N(E) = 2 \times \left(\frac{\pi n}{2} dn \right) \frac{1}{L^2 dE} = \frac{m}{\pi \hbar^2}, \quad (1-6)$$

where n and dn is the same as in Eq. 1-2 and 1-3.

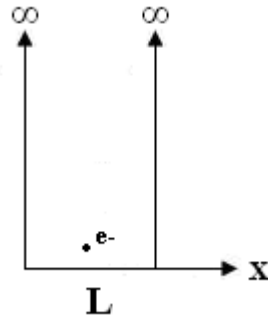


Figure 1-2. An electron is confined in 1-D box.

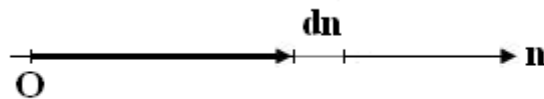


Figure 1-3. Schematic diagrams of the density of states in 1-D system.

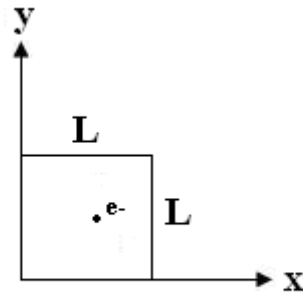


Figure 1-4. An electron is confined in 2-D box.

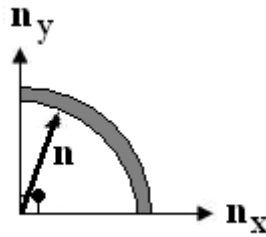


Figure 1-5. Schematic diagrams of the density of states in 2-D system.

For a three-dimensional system, we consider an electron confined in a three-dimensional box as shown in figure 1-6, and the energy level for the electron is

$$E = \frac{\hbar^2}{2m} (n_x^2 + n_y^2 + n_z^2) \equiv \frac{\hbar^2}{2m} n^2, \quad (1-7)$$

where n_x , n_y , and n_z are positive integers. In a three-dimensional system as shown in figure 1-7, the density of states could be written as

$$N(E) = 2 \times \left(\frac{4 \pi n^2}{8} dn \right) \frac{1}{L^3 dE} = \frac{\sqrt{2} m^{3/2}}{\hbar^3 \pi^2} \sqrt{E}. \quad (1-8)$$

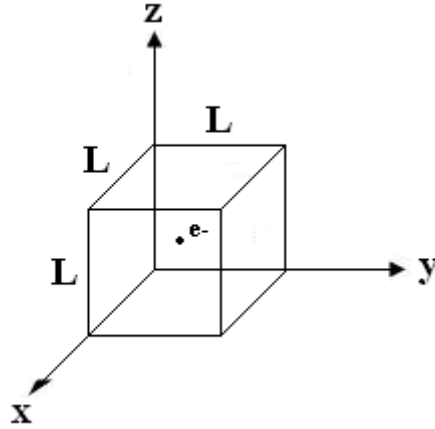


Figure 1-6. An electron is confined in 3-D box.

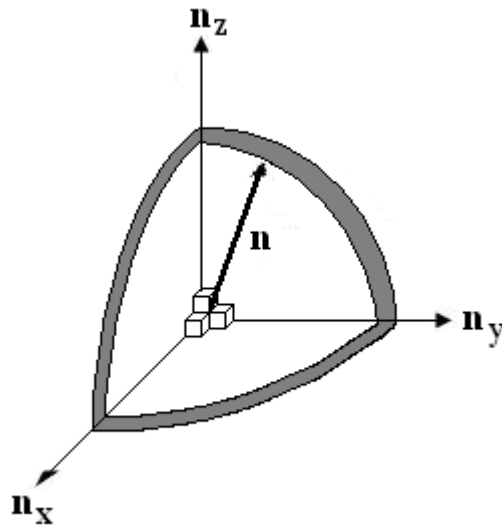


Figure 1-7. Schematic diagrams of the density of states in 3-D system.

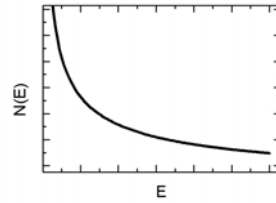
From the derivation above, we could write down the density of states in one-, two-, and three-dimensional system respectively as follows:

$$N_{1D}(E) = \frac{\sqrt{2m}}{\pi \hbar} \frac{1}{\sqrt{E}}, \quad (1-9)$$

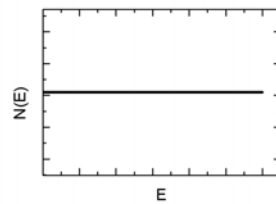
$$N_{2D}(E) = \frac{m}{\pi \hbar^2}, \quad (1-10)$$

$$N_{3D}(E) = \frac{\sqrt{2m}^{3/2}}{\hbar^3 \pi^2} \sqrt{E}. \quad (1-11)$$

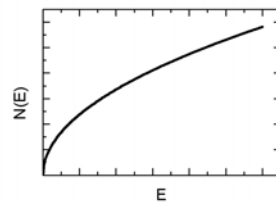
We can see that two-dimensional density of states is independent of E . Figure 1-8 shows the comparison between these three densities of states.



(a)



(b)



(c)

Figure 1-8. Variation of the energy dependence for the density of states in (a) one-dimensional, (b) two-dimensional, and (c) three-dimensional system.

1-3 AlGaN/GaN electron system

The behavior of electrons confined at the interface of AlGa_xN and GaN is an example of the two-dimensional electron gas system. As mentioned earlier, due to the different band-gaps of AlGa_xN and GaN, there will be a triangular potential well at the interface of AlGa_xN and GaN, forming a two-dimensional electron gas. Recently, there have been a lot of experimental and theoretical studies on AlGa_xN/GaN system. It has been shown that there exist spontaneous polarization and piezoelectric polarization in such a system [1]. The spontaneous polarization is due to

the non-coincidence of the centers of the cations and anions when they are in the lowest energy states, and the piezoelectric polarization is due to lattice mismatch strain and thermal strain caused by the difference in the thermal expansion coefficients of the AlGa_{1-x}N_x and GaN layers as shown in figure 1-9. Because of such polarization in AlGa_{1-x}N_x and GaN, there exist sheet charges at the AlGa_{1-x}N_x/GaN interface, as given by

$$\sigma = (P_{SP} + P_{PE})_{AlGaN} - (P_{SP})_{GaN} \quad (1-12)$$

Therefore, if the sheet charges are positive, free electrons will have to compensate for them during the cooling process after growth. In addition, many theories and experiments show that upon increasing the Al content or the thickness of AlGa_{1-x}N_x, the piezoelectric and spontaneous polarization of AlGa_{1-x}N_x will increase accordingly. Hence more electrons will be confined here and the two-dimensional carrier density will increase [1-4]. In chapter 4, we study the electrical transport in AlGa_{1-x}N_x/GaN system with different Al-contents. In chapter 5, we study how the Si₃N₄ film grown below the GaN layer can affect the two-dimensional electron transport.

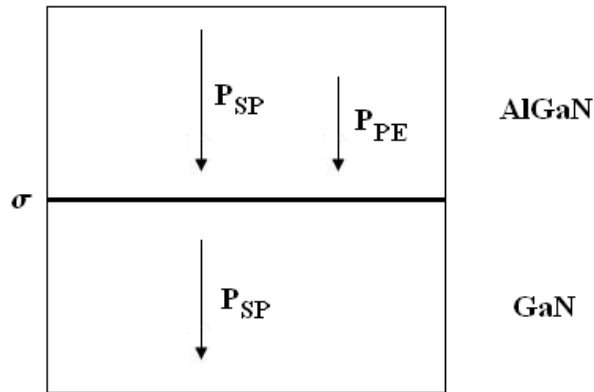


Figure 1-9. The polarization distribution of AlGa_{1-x}N_x and GaN.

1-4 Ohmic contact

Before performing a transport experiment, it is important to carefully consider the kind of metal to use for the contact. In addition, one must also take into account whether the contact will behave as an ohmic contact in the experiment with this particular choice of metal.

The easiest way to think of an ohmic contact is that of the ohmic contact as a black body which will absorb and emit energy in equal

portions while energies pass through it. If the contact is ohmic, there will be no voltage drop when current passes through the contact.

However, in most experiments, there will be a Schottky barrier between the semiconductor and metal. Therefore, when the current passes through the contact in one direction, the voltage drop will not be the same as when the current passes through in the opposite direction. (It should be the same, but it is not.) This is the simplest way to check if the contact is ohmic or non-ohmic. For a successful and reliable experiment, we need to make sure that the contact is ohmic.

References

1. O. Ambacher, J. Smart, J. R. Shealy, N. G. Weimann, K. Chu, M. Murphy, W. J. Schaff, and L. F. Eastman, *J. Appl. Phys.* **85**, 3222 (1999).
2. I. P. Smorchkova, C. R. Elsass, J. P. Ibbetson, R. Vetury, B. Heying, P. Fini, E. Haus, S. P. DenBaars, J. S. Speak, and U. K. Mishra, *J. Appl. Phys.* **86**, 4520 (1999).
3. R. Dimitrov, M. Murphy, J. Smart, W. Schaff, J. R. Shealy, L. F. Eastman, O. Ambacher, and M. Stutzmann, *J. Appl. Phys.* **87**, 3375 (2000).
4. H. W. Jang, C. M. Jeon, K. H. Kim, J. K. Kim, S.-B. Bae, J.-H. Lee, J. W. Choi, and J.-L. Lee, *Phys. Stat. Sol. (b)* **228**, 621 (2001).

Chapter 2

Theoretical Background

2-1 Hall effect

2-1-1 Introduction

When we obtain a semiconductor sample, it is important to know precisely the type of carriers present, namely, whether the carriers are positively charged holes or negatively charged electrons. However, if we only measure the direction of flow of the current, we would not be able to distinguish between the two types of carriers. Fortunately, in 1879 a physicist Edwin Hall invented a method to measure not only the type of carriers, but also the carrier concentration.

This measurement is known as the “Hall measurement,” and it is the most commonly used method to determine the type of carrier in a sample as well as the carrier concentration. In this thesis, we made frequent use of the Hall measurement to determine the carrier concentration of our sample.

2-1-2 Theoretical derivation for 3-dimension

Let us consider a bulk sample as shown in figure 2-1. The sample was connected at opposite ends with a battery with potential difference V , and on the two sides with a voltage meter. We first assume that the carriers are electrons. When we turn on a magnetic field B homogeneously around the sample along the positive x -axis, the carriers that pass through the sample would experience a Lorentz force \mathbf{F}_B induced by their velocities and the background magnetic field,

$$\mathbf{F}_B = -e \mathbf{v}_d \times \mathbf{B} = e v_d \hat{B} \hat{z}. \quad (2-1)$$

Initially, the carriers in the sample will tend to accumulate on one side and leave the other side oppositely charged as shown in figure 2-2(a). Therefore the remaining carriers will experience not only a magnetic Lorentz force but also an electric Lorentz force induced by the side accumulation charges. Before these two forces are balanced, the accumulation charges will increase little by little. When the electric force exactly cancels out the magnetic force, the charge accumulation will cease, and the carriers will flow through the sample as if no magnetic background has been applied, as shown in figure 2-2(b).

However, there is a salient feature left in the sample which will enable us to determine the type of carriers present as well as their concentration. The key is the voltage across the sides. Assuming now that the carriers in the sample are oppositely charged, i.e., that they are positively charge holes as shown in figure 2-2(c), without changing the direction of the current; one can see that the carriers will still accumulate on the same side of the sample. However, if we measure the voltage across the two sides, we will discover that the sign of the side voltage is reversed. This startlingly simple result tells us that we can simply measure the sign of the voltage meter to determine the type of carriers in the sample.

Furthermore, in addition to determining the type of carriers present, the Hall measurement can also tell us the carrier concentration if we calculate the side voltage quantitatively.

Without loss of generality, we can assume that the carriers are electrons. When the electric force is equivalent to the magnetic force, this electric field is often known as the Hall electric field E_H . The carriers will pass through the sample as if no background magnetic field exists. In this case,

$$\mathbf{F}_{\text{Lorentz}} = \mathbf{F}_E + \mathbf{F}_B = -e E_H \hat{\mathbf{z}} + e v_d \mathbf{B} \hat{\mathbf{z}} = \mathbf{0}, \quad (2-2)$$

$$E_H \equiv \frac{V_H}{w} = v_d B. \quad (2-3)$$

And from the Drude model, we have

$$\mathbf{J} = e n v_d, \quad (2-4)$$

$$v_d = \frac{\mathbf{J}}{e n} = \frac{\mathbf{I}}{w d e n}. \quad (2-5)$$

Combining these two equations, we can get

$$V_H = \frac{I}{e d n} B, \quad (2-6)$$

$$R_H \equiv \frac{V_H}{I} = \frac{1}{e d n} B. \quad (2-7)$$

The constant R_H is known as the Hall coefficient, and it is proportional to the applied magnetic field and inversely proportional to the carrier concentration. From the above derivation, we see that the sample will be p-type if R_H is negative, and n-type if R_H is positive. However, if we reverse the connection of voltage meter, the answers will be reversed. It all depends on the connection configuration of the voltage meter.

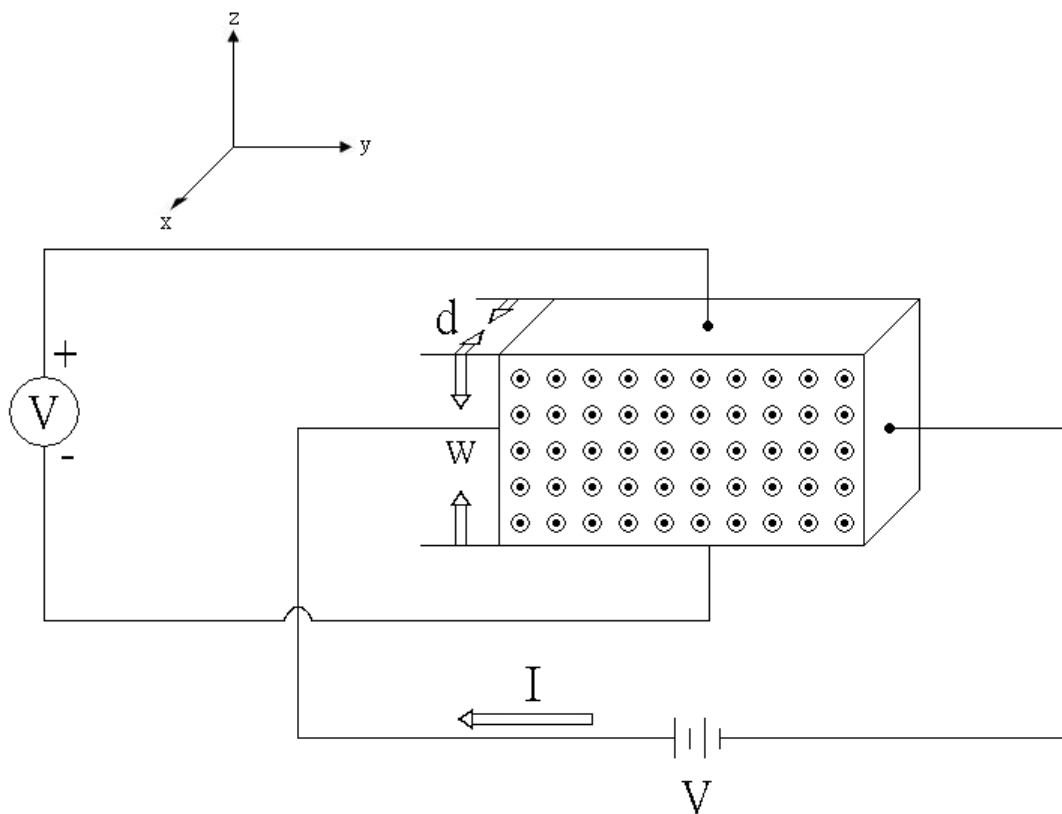
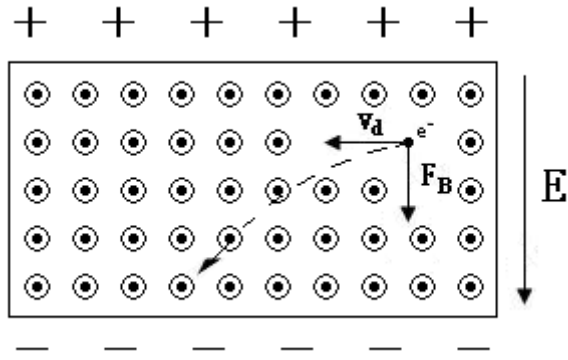
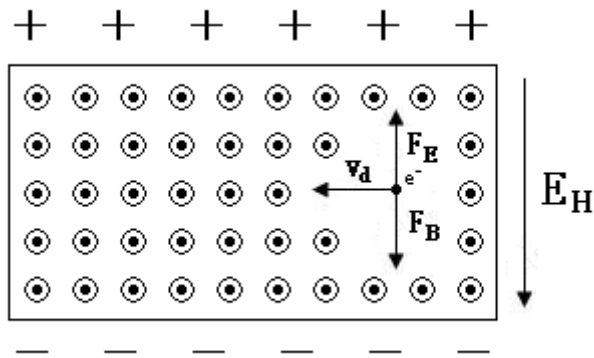


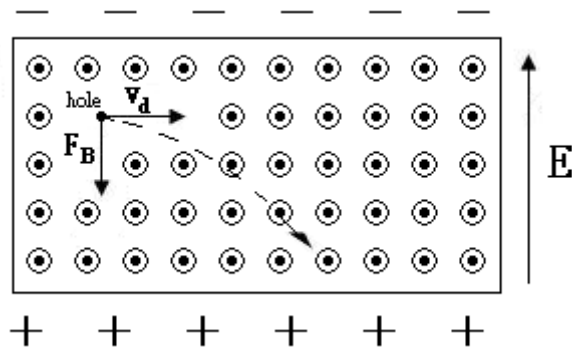
Figure 2-1. Schematic of the instrument set-up for the classical Hall effect.



(a)



(b)



(c)

Figure 2-2. (a) When the electron passes through the sample, it will experience a magnetic Lorentz force, and will then tend to move downwards so as to accumulate at the bottom of the sample. (b) The electrons will continue to accumulate until they produce an electric field equal and opposite to the magnetic field acting on the remaining electrons. (c) If the carriers are holes, they will bend in the same direction just as the electrons do, but when we measure the side voltage, the sign of Hall potential will be reversed.

2-1-3 Two-dimensional Hall effect

In some special cases, the electrons in the sample may be forbidden to move in the direction along the z-axis, and are thus confined to move in just one plane. Such a system is known as a two-dimensional system. There are several interesting physical properties in a two-dimensional system. For example, the density of state is independent of the energy. Here, we devote a little attention to investigating how it will affect the Hall effect if the system is two-dimensional.

Following previous derivations, we see that Eq. 2-1, 2-2, and 2-3 are all independent of the system dimension. For Eq. 2-4, the current density, is dependent on the system dimension. So Eq. 2-5 will be modified to

$$v_d = \frac{J}{en} = \frac{I}{wen}, \quad (2-8)$$

because the system does not have the concept of ‘depth’. Combining Eq. 2-8 and 2-3, we get

$$V_H = \frac{I}{en} B, \quad (2-9)$$

$$R_H \equiv \frac{V_H}{I} = \frac{1}{en} B. \quad (2-10)$$

Comparing Eq. 2-7 and 2-10, we see that if we assume that the depth of three-dimensional system is one unit, the problem for three dimensions will be reduced to two dimensions. Similar techniques will be used in the following section. We will discuss the three-dimensional van der Pauw equation. By setting the depth equal to one, we reduce the system to a two-dimensional problem.

2-1-4 Experimental techniques

In real life, it is almost impossible to measure the exact Hall coefficient. Figure 2-3 shows such an example. In this case, the positions of the four contacts are arbitrary. From the above derivations, if we do not turn on the magnetic field, we will measure the value of R_H to be zero. As a matter of fact, we may obtain a nonzero R_H if we do not turn on the magnetic field. This happens because the direction of voltage meter may

not be perfectly perpendicular to current flowing. Consequently, the voltage meter will not only measure the Hall resistance, but also the resistance parallel to the direction of current. Thus, we could rewrite our equation as

$$R_{xy}(B) = R_H(B) + R_{xx} = \frac{1}{d e n} B + R_{xx}, \quad (2-11)$$

where R_{xx} is independent of magnetic field.

On the other hand, in order to minimize experimental errors, it is better to determine the carrier concentration by more consistent measurements. From Eq. 2-11, we know that if we measure R_{xy} under different magnetic fields, and perform linear fitting on R_{xy} with respect to B , the fitting slope will be $\frac{1}{d e n}$. By substituting the depth and electric charge of the sample into this slope, we can calculate the carrier concentration of the sample. In experiments, the R-squared of this fit could easily exceed 0.999. Figure 2-4 shows an example of the Hall measurement.

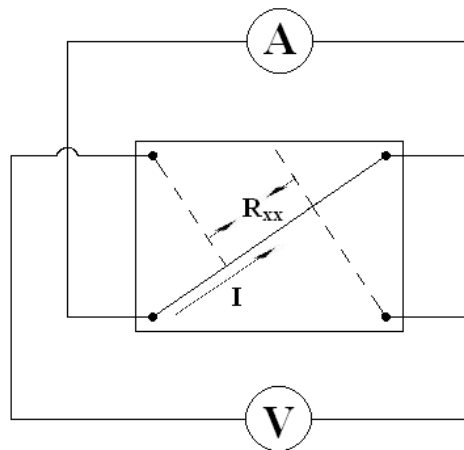


Figure 2-3. A draft of a real four-points measurement case.

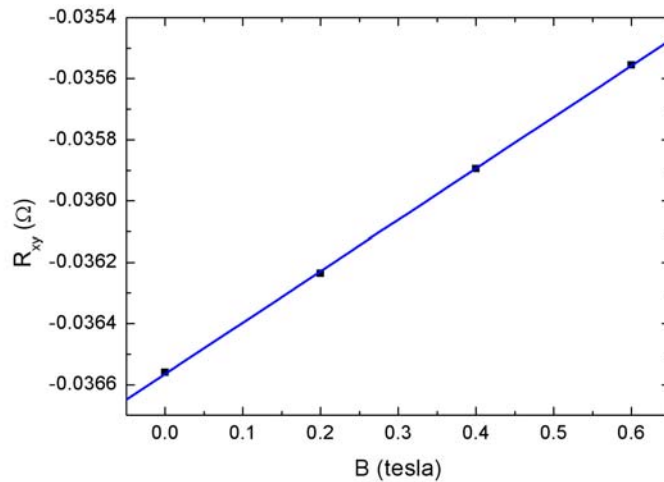


Figure 2-4. A case of GaAs Hall measurement where the depth is $350 \mu\text{m}$. By linear fitting of R_{xy} with respect to B , $R_{xy} = -0.03656 + 0.00168 B$, $R^2 = 0.9997$ where the slope is $0.00168 = \frac{1}{d e n}$. By substituting the depth of GaAs and electric charge into the equation, we can obtain the carrier density $n = 1.06 \times 10^{19} \text{ cm}^{-3}$.

2-2 Classical Drude model

In 1900, Drude developed an electron theory of electrical and thermal conduction in metals. Surprisingly, while the electrons were discovered by J. J. Thomson in 1897, it was not until 1911 that Millikan was able to measure the electron charge. Before this, Drude had already used this model (where there are plenty of electrons in a material) and kinetic theory to predict the electrical and thermal properties of metals. Although the assumptions of his theories were subsequently shown to be not entirely correct, it did predict accurately the electrical and thermal conductivity of a metal. We now look at his four assumptions:

- (1) Between collisions the electrons move in straight lines and are not influenced by the heavy positive ions.
- (2) The collisions are instantaneous events like rubber balls bouncing off a heavy fixed mass, which abruptly alter the velocity of the electrons.

- (3) The electrons lose all the extra energy gained from the applied field upon collision.
- (4) The average distance an electron travels between collisions (the mean free path in kinetic theory) is of the order of the distance apart of the fixed ions (the lattice separation).

With these four assumptions, one can estimate the conductivity of a metal from classical theories. First, assume that there are lots of electrons moving freely in a metal and experiencing an external applied electric field. According to Ohm's Law, there will be a current through the metal parallel to electric field.

$$\mathbf{J} = \sigma \mathbf{E}. \quad (2-12)$$

If the metal contains n conduction electrons per unit volume and each electron carrying charge $-e$ with drift velocity \mathbf{v}_d , we have

$$\mathbf{J} = -n e \mathbf{v}_d. \quad (2-13)$$

However, in an external electric field \mathbf{E} , each electron experiences a force $-e \mathbf{E}$ and thus has acceleration $-\frac{e}{m} \mathbf{E}$. We can write the velocity of electrons in metal as

$$\mathbf{v} = \mathbf{v}_0 - \frac{e}{m} \mathbf{E} t, \quad (2-14)$$

where \mathbf{v}_0 is the initial velocity of an electron just after collision. On the average, we have

$$\langle \mathbf{v} \rangle = \langle \mathbf{v}_0 \rangle - \left\langle \frac{e}{m} \mathbf{E} t \right\rangle = \langle \mathbf{v}_0 \rangle - \left(\frac{e}{m} \mathbf{E} \right) \tau, \quad (2-15)$$

where τ is the average time between collisions and is often called the mean free time, or relaxation time. In addition, electrons moving in metals are scattered randomly, so it is reasonable to assume that $\langle \mathbf{v}_0 \rangle = 0$, thus

$$\langle \mathbf{v} \rangle = - \left(\frac{e}{m} \mathbf{E} \right) \tau. \quad (2-16)$$

This is the drift velocity, and substituting into Eq. 2-13, we get

$$\mathbf{J} = \frac{n e^2 \tau}{m} \mathbf{E}. \quad (2-17)$$

Comparing with Eq. 2-12, we can express the conductivity in terms of the

intrinsic properties of the metal.

$$\sigma = \frac{n e^2 \tau}{m}. \quad (2-18)$$

Furthermore, in semiconductors there is a quantity that is more convenient than the conductivity. That quantity is the mobility μ :

$$\mu \equiv \frac{|\mathbf{v}_d|}{|\mathbf{E}|} = \frac{e}{m} \tau. \quad (2-19)$$

In a metal, the carrier density is always temperature-independent. So we can compare the scattering rates at different temperatures by the conductivity. However, in a semiconductor, the carrier density changes with temperature, thus the mobility could describe the scattering rates more accurately. This is why the mobility is more commonly used in a semiconductor device.

2-3 Van der Pauw measurement

2-3-1 Introduction

As mentioned previously, when we obtain a sample, we are often interested in its carrier concentration. However, another important physical quantity of interest is the resistivity. Figure 2-5 illustrates a way to determine a sample's resistivity. However, it is not convenient for use in certain cases. For example, our sample may be circular, triangular or any other shape as shown in figure 2-6. In such cases, it is hard to determine the sample's resistivity. Fortunately, in 1958 van der Pauw published a convenient theory for calculating the resistivity for a material of any shape [1].

Before applying this theory, there are four points that need to be noted:

- (1) The contacts are on the circumference of the sample.
- (2) The contacts are sufficiently small.
- (3) The sample is homogeneous in thickness.

(4) The surface of the sample is singly connected, i.e., the sample does not have isolated holes.

As shown in figure 2-6, we apply a current which goes through contact A and leaves through contact B, and measure the potential difference between contact C and D. Next, we divide it by the applied current—and call it $R_{AB,CD}$. Similarly, we apply a current which flows through contact B and exits via contact C, measure the potential difference and divide it by the applied current, calling it $R_{BC,DA}$. According to van der Pauw’s theory, we have that

$$e \frac{\pi d R_{AB,CD}}{\rho} + e \frac{\pi d R_{BC,DA}}{\rho} = 1. \quad (2-20)$$

Solving Eq. 2-20, we can determine the resistivity of the sample. Although the equation seems much more complicated than before, we can apply it on any sample without caring for the shape of the sample and the displacements between the contacts. This would prove very handy in experiments.

Note: Eq. 2-20 applies to a three-dimensional system. For the case of a two-dimensional system, we can ignore d , and set $d = 1$.

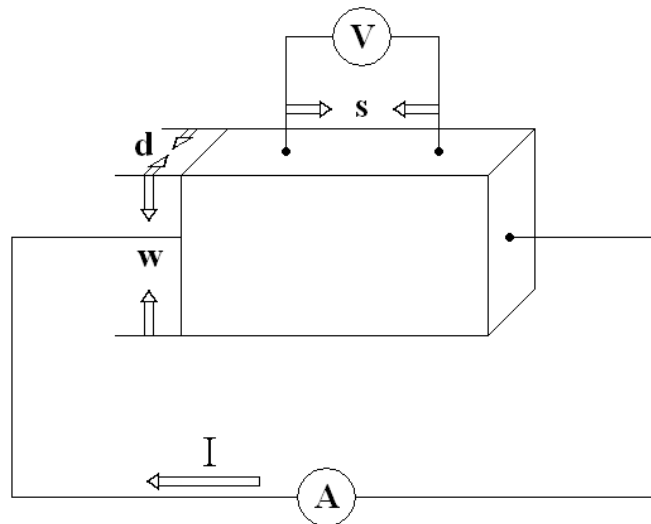


Figure 2-5. The classical idea for measuring the resistivity of a sample.

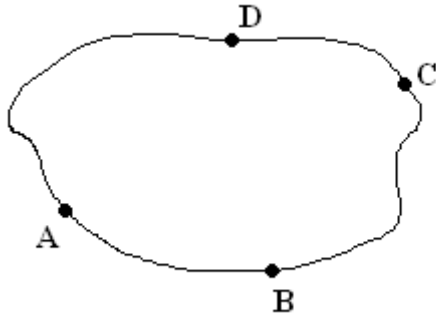


Figure 2-6. Four-point measurements for a sample of any shape.

2-3-2 Theoretical derivation

Before considering a sample of arbitrary shape, we first derive our equation for the infinite plane. By conformal mapping, we can then generalize our derivation to a sample of arbitrary shape.

As shown in figure 2-7, the placements of the contact A, B, C, and D, are arbitrary. Since our sample is homogeneous, when we apply a current to contact A, we can assume that the current is uniformly spread out into the sample to infinity as shown in figure 2-7. From the classical Drude model, we have

$$\mathbf{J} = \sigma \mathbf{E} = \frac{1}{\rho} \mathbf{E}, \quad (2-21)$$

and

$$\pi r d J = I, \quad (2-22)$$

because we have assumed that the current is uniformly spread out into the sample. We can then calculate the electric field in the sample with respect to contact A:

$$\mathbf{E} = \frac{\rho I}{\pi d} \frac{1}{r} \hat{\mathbf{r}}. \quad (2-23)$$

From Eq. 2-23, we can calculate the potential difference between contact C and D:

$$V_D - V_C = - \int_{r_c}^{r_b} \mathbf{E} \cdot d\mathbf{r} = - \frac{\rho I}{\pi d} \ln \frac{\alpha + \beta + \gamma}{\alpha + \beta}. \quad (2-24)$$

Likewise, we assume that the current converges uniformly from infinity to contact B. We can calculate the potential difference due to this current:

$$V_D - V_C = -\frac{\rho I}{\pi d} \ln \frac{\beta}{\beta + \gamma}. \quad (2-25)$$

Combining the contributions of contact A and B, we see that when we apply a current entering through contact A and exiting through contact B, the potential difference between them is given by

$$V_D - V_C = -\frac{\rho I}{\pi d} \ln \frac{\alpha + \beta + \gamma}{\alpha + \beta} \frac{\beta}{\beta + \gamma}. \quad (2-26)$$

Dividing it by the current I:

$$R_{AB,CD} = -\frac{\rho}{\pi d} \ln \frac{\alpha + \beta + \gamma}{\alpha + \beta} \frac{\beta}{\beta + \gamma}. \quad (2-27)$$

Similarly, when we apply a current entering through contact B and exiting through contact C, the potential difference between contact B and C is

$$R_{BC,DA} = -\frac{\rho}{\pi d} \ln \frac{\alpha}{\beta + \gamma} \frac{\gamma}{\alpha + \beta}. \quad (2-28)$$

In addition, we know that

$$\frac{\alpha + \beta + \gamma}{\alpha + \beta} \frac{\beta}{\beta + \gamma} + \frac{\alpha}{\beta + \gamma} \frac{\gamma}{\alpha + \beta} = 1. \quad (2-29)$$

Combining Eq. 2-27, 2-28, 2-29, we obtain van der Pauw's equation.

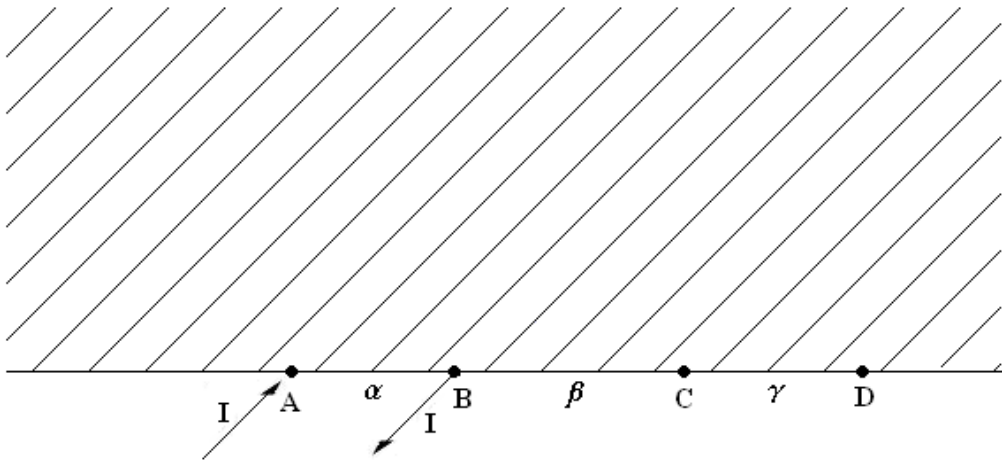


Figure 2-7. Consider a sample with the shape of a semi-infinite plane.

2-3-3 Contact displacement errors

Van der Pauw had provided a useful method to measure the resistivity of sample without considering its shape. However, four theoretical conditions need to be satisfied for the method to be valid. One of the conditions is that the contacts need to be on the boundary of the sample. However, when performing four-point measurements, it is difficult to locate our contacts exactly at the boundary and impossible to reduce it to a point on the sample surface. Consequently, some experimental errors are inevitable. Here we consider the case where one of our contacts is located a little inside boundary, and calculate the relative error in the resistivity for this case [2, 3].

Consider the same configuration as that in figure 2-8. Before deriving our result, we make the simplification that our sample is shaped like a semi-infinite plane, as shown in figure 2-9, and that there is a conformal mapping relation between the two shapes,

$$w = \frac{i - z D}{i + z 2}. \quad (2-30)$$

As mentioned earlier, we can calculate the potential difference between contacts C and D:

$$V_D - V_C = -\frac{\rho I}{\pi d} \ln\left(\frac{a + 2}{\sqrt{(a + 1)^2 + \Delta^2}} \frac{\sqrt{1 + \Delta^2}}{2}\right), \quad a \rightarrow \infty. \quad (2-31)$$

Therefore,

$$R_{AB,CD} = \frac{\rho}{\pi d} \ln \frac{2}{\sqrt{1 + \Delta^2}}. \quad (2-32)$$

In addition, if we assume our contact to be on the boundary (even though it was actually located in the interior of the sample), by van der Pauw's method, we could obtain another relation between $R_{AB,CD}$ and resistivity.

$$R_{AB,CD} = \frac{\rho'}{\pi d} \ln 2. \quad (2-33)$$

By equating Eq. 2-32 and 2-33, we can derive the relation between the relative error for the resistivity and the contact displacement error.

$$\frac{\rho' - \rho}{\rho} = \frac{\Delta \rho}{\rho} = -\frac{\ln(1 + \Delta^2)}{2 \ln 2}. \quad (2-34)$$

This is the equation for the error correction for a sample shaped like a semi-infinite plane. Now we can apply conformal mapping to transform our result to a circular shape. By conformal mapping we could describe the positions of contacts C and C' by the following relation.

$$\frac{D}{2} - d = \frac{i - i\Delta}{i + i\Delta} \frac{D}{2}. \quad (2-35)$$

Thus, we can write Δ in terms of d

$$\Delta = \frac{d/D}{1-d/D}. \quad (2-36)$$

Substituting into Eq. 2-34, we get

$$\frac{\Delta\rho}{\rho} = - \frac{\ln\left[1 + \left(\frac{d/D}{1-d/D}\right)^2\right]}{2 \ln 2}, \quad (2-37)$$

which represents the error correction of the circular shape without any approximation. But for convenience, we can do some approximation for $\frac{d}{D} \ll 1$, then Eq. 2-37 would be modified as such:

$$\frac{\Delta\rho}{\rho} = - \frac{1}{2 \ln 2} \left(\frac{d}{D}\right)^2 \approx - 0.722 \left(\frac{d}{D}\right)^2. \quad (2-38)$$

From the above equation, we can see that although the contact displacement does indeed affect our calculation of the resistivity, it will not seriously affect our result. If we make our sample size larger, we could reduce the relative error due to contact displacement, as predicted intuitively.

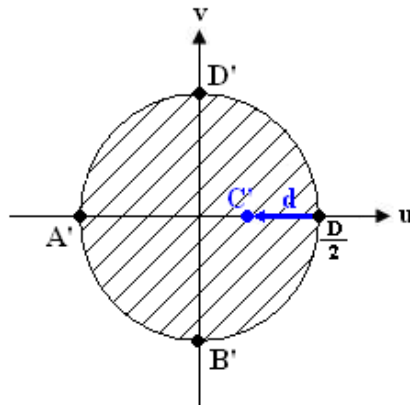


Figure 2-8. Assuming that our sample is circular in shape, we calculate the contact displacement errors when the diameter of the circle is D and the contact C' is a distanced d to the left of its original position.

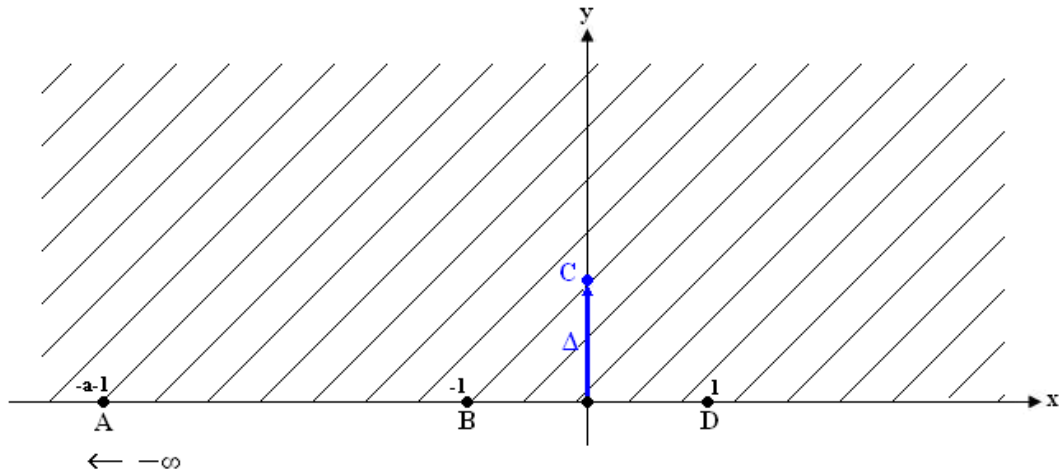


Figure 2-9. Before assuming that our sample is circular, we first assume our sample to be a semi-infinite plane. We subsequently transform our result to the circular problem.

2-3-4 Practical application

Up till now, we have learned that the van der Pauw method could be used to determine the resistivity of the sample without taking into account the shape of the sample. However, we do not yet know how to solve this equation because it does not have analytic solutions. Therefore, it is important to better understand the behavior of this equation in order to solve this equation more accurately.

Here, we have derived van der Pauw's equation. For convenience, we rewrite van der Pauw's equation as

$$e^{-ax} + e^{-bx} = 1, \quad (2-39)$$

where a and b are positive numbers. Thus our problem is to solve for x in this equation. We can define a function

$$f(x) = e^{-ax} + e^{-bx} - 1. \quad (2-40)$$

And our x must satisfy $f(x)=0$, namely it is the root for $f(x)$. In addition, we could analyze the behavior of $f(x)$ to better understand our problem.

First, we could see that $f(0)=1$ and $f(\infty)=-1$. We can infer that there is at least one root for $f(x)=0$ between zero and infinity. Furthermore, we

can take the derivative of $f(x)$ with respect to x .

$$f'(x) = -a e^{-ax} - b e^{-bx}. \quad (2-41)$$

Because a and b are positive numbers, we can know that $f'(x) < 0$ for all x , so $f(x)$ is a monotonically decreasing function of x . Combining the above two deductions, we can conclude that there is only one positive root for $f(x)=0$. Figure 2-10 depicts a case of $f(x)$ where $a=1$ and $b=2$.

After understanding the behavior of $f(x)$, there are various methods for calculating the root for $f(x)$. The most famous and useful method is Newton's method. We could use successive iteration to approach our root to any accuracy we desire. In this thesis, I wrote a Matlab program using "WHILE LOOP" to approach the root for $f(x)=0$, and take the reciprocal of x to obtain the resistivity.

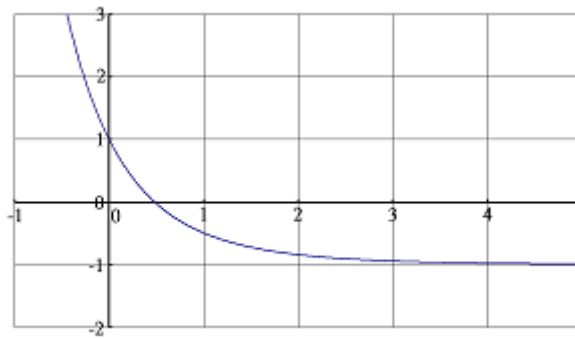


Figure 2-10. $f(x) = e^{-ax} + e^{-bx} - 1$, where $a=1$ and $b=2$.

References

1. L. J. Van der Pauw, Philips Research Report No. **13**, 1 (1958).
2. Daniel W. Koon, Rev. Sci. Instrum. **60**, 271 (1989).
3. Daniel W. Koon, Arshad A. Bahl, and Edward O. Duncan, Rev. Sci. Instrum. **60**, 275 (1989).

Chapter 3

Experimental Instruments

3-1 Close cycle system

3-1-1 Introduction

Before performing Hall measurements, we often measure our samples in our close cycle system. This is the simplest way to check if the sample contacts will fail at low temperatures and we can measure the resistance of the sample from room temperature to low temperatures.

In some cases, the measured resistance might have unexpected jumps. In such cases, the contacts may have failed at low temperatures. In addition, it takes very little time to complete this experiment, and the process is simple and straightforward. Hence, we often test sample contacts and resistance behavior before performing the actual Hall effect measurement.

3-1-2 Close cycle device

The devices used in this experiment are quite simple. There is a Keithley 199 for four-point measurement, a Lakeshore 330 for measuring the sample temperature, a mechanical pump for pumping the vacuum chamber, and a refrigerator to lower the temperature of the system. Lastly, we connect the Keithley 199 and the Lakeshore 330 to a computer for recording the data automatically. Figure 3-1 shows the setup for this system.

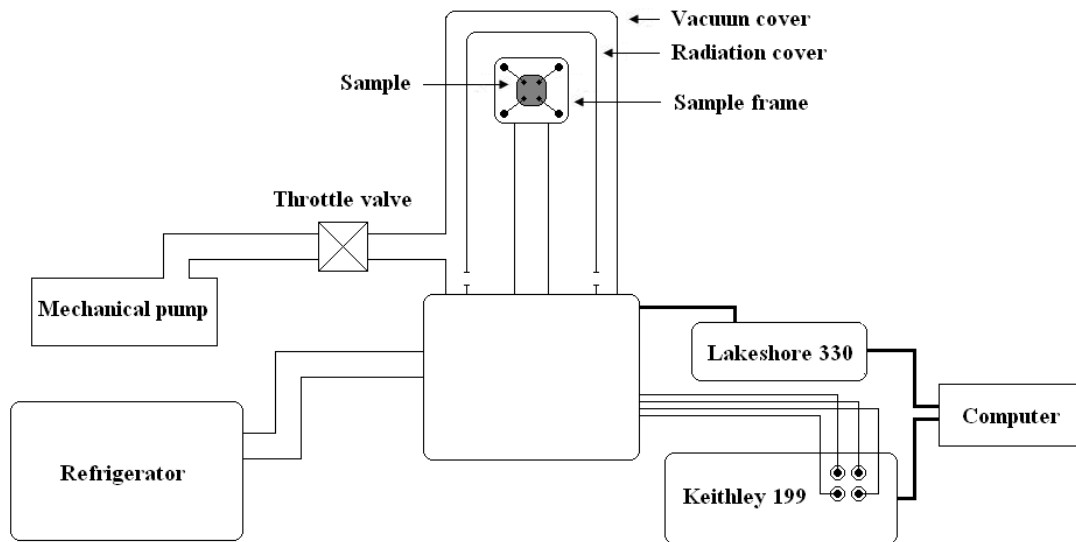


Figure 3-1. The diagram of a close-cycle system.

3-1-3 Experimental steps

There are sixteen steps involved in performing an experiment in a close cycle system.

- (01) Stick the sample on the sample frame with twin adhesive, and connect the connection wires on the frame.
- (02) Turn on the Lakeshore 330 and Keithley 199 to check if the temperature and resistance is normal.
- (03) Close the radiation cover and vacuum cover.
- (04) Open the throttle valve, which is connected to the mechanical pump.
- (05) Turn on the mechanical pump, and pump the chamber for one hour.
- (06) Turn on the compressor bottom of the refrigerator to warm it for thirty minutes.
- (07) Close the throttle valve, and then turn off the mechanical pump.
- (08) Turn on the computer and start the “Low Temperature Resistance” program on the desktop.
- (09) Input the file name on the program front panel.
- (10) Run the program.
- (11) Turn on the cold head bottom of the refrigerator to lower the temperature.

- (12) The program will record the resistances and temperatures automatically until the temperature is below 9.8 K. After 9.8 K, the program will stop recording data automatically.
- (13) Wait about half an hour, the temperature will drop below 10 K.
- (14) Turn off the cold head bottom of the refrigerator, and then turn off the compressor bottom of the refrigerator.
- (15) Turn off the Lakeshore 330, the Keithley 199, and the computer.
- (16) The experiment is completed.

3-2 Hall effect system

3-2-1 Introduction

In solid-state physics, it is important to know the carrier concentration and resistivity of a sample. Measuring them at room temperature is simple and relatively straightforward. However, in some general cases, we want to know how the carrier concentration and resistivity varies with temperature. Here, we can perform these measurements with our Hall effect system. After a lengthy eight hours measurement, one can obtain the carrier concentration, resistivity, and mobility with respect to temperature. On further analysis of these measurements, we can gain a better understanding of the behavior of phonons with respect to temperature, the quality of sample, the activation energy, etc. Although this experiment is simple, it provides a lot of extremely useful and practical information on the sample.

3-2-2 Hall measurement device

Although the theory seems quite simple, it is extremely complicated and difficult to complete the experiment. First of all, one needs a magnetic device which can provide a maximum magnetic field of 8000 gauss. We also need a Keithley 2000 for measuring voltage drop of the sample, as well as a Keithley 224 for the current flowing through the sample. Next, a LTC-11 is needed to measure the temperature of the sample. In addition, there is also a relay box to control the directions of current through the sample and the direction for measuring voltage drop. Figure 3-2 shows the eight modes we used in the experiment.

On top of these, we also need to infuse helium gas into the inner chamber for exchanging heat, and liquid helium into the medium chamber to lower the temperature of the system to around 4 K. Here, we make use of a transfer tube to infuse liquid helium into the medium chamber. Lastly, we need to connect Keithley 2000, Keithley 224, LTC-11 and the relay box to a computer to switch the relay box and record the data automatically. Figure 3-3 shows the diagram of this system.

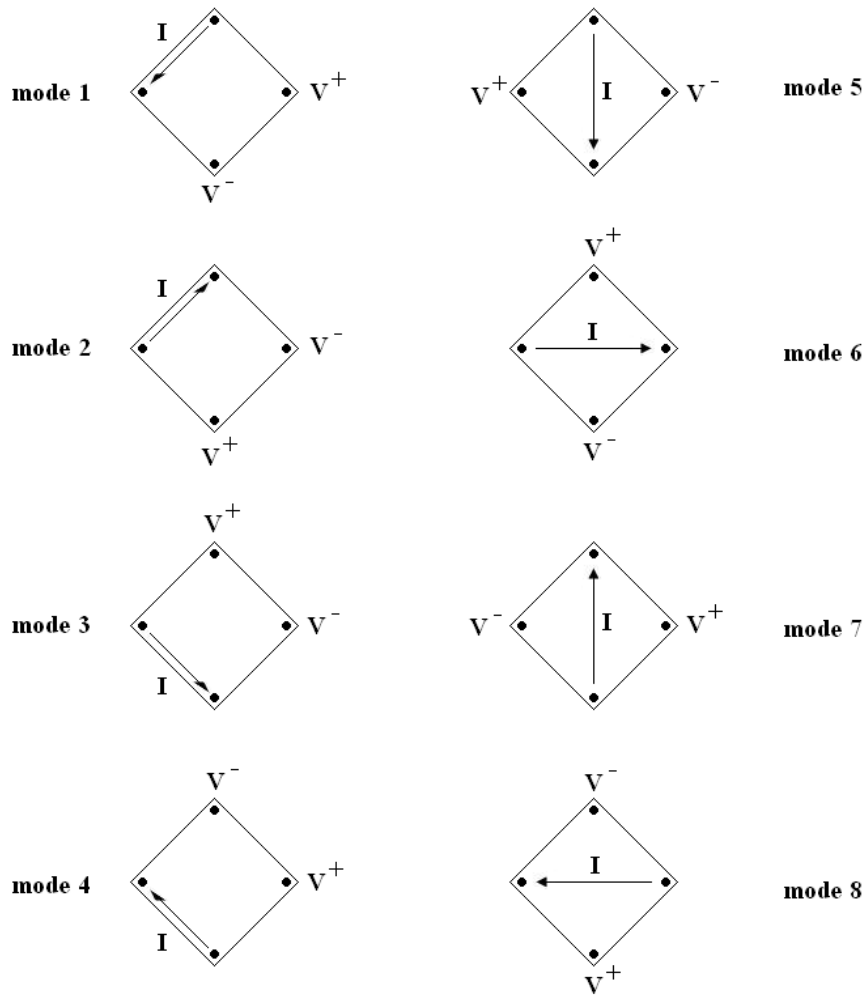


Figure 3-2. The eight modes of Hall measurement.

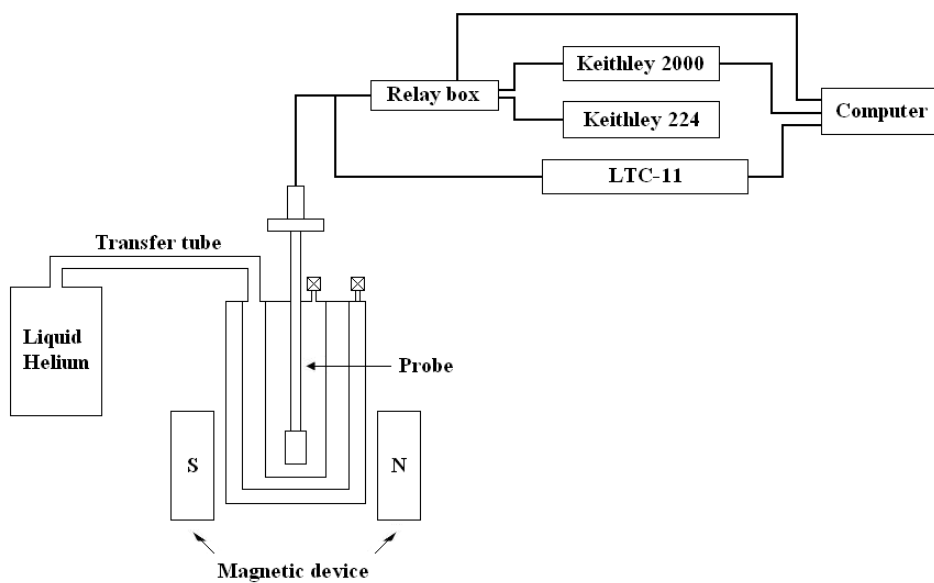


Figure 3-3. The diagram of Hall effect system.

3-2-3 Experimental steps

There are thirty-three steps when performing an experiment in a Hall effect system.

- (01) Stick the sample on the probe with twin adhesive, and connect the connection wires on the probe.
- (02) Connect the probe to the computer and insert the probe into the chamber.
- (03) Turn on the Keithley 2000, Keithley 224, and LTC-11.
- (04) Turn on the computer to check if the contact is ohmic.
- (05) Use the mechanical pump and the turbo pump to pump the transfer tube to below 5×10^{-4} torr.
- (06) Pump the outer chamber to lower than 5×10^{-4} torr.
- (07) Pump the inner chamber to lower than 5×10^{-4} torr.
- (08) Use the helium gas bottle to infuse a little helium gas into the inner chamber.
- (09) Insert the transfer tube into the liquid helium bottle.
- (10) Connect the transfer tube to the medium chamber in order to infuse liquid helium into it for lowering temperature.
- (11) Start “New Hall measurement” program on the desktop. (Dubbed “New” because I rewrote the program to be more convenient.)
- (12) Input the file name and the parameters of waiting time and the switching time of the relay box in the program.
- (13) Determine the proper current size that needs to be input into the sample. And then enter it into the Keithley 224.
- (14) Turn on the cooling water and then turn on the magnetic device.
- (15) Adjust the magnetic device to provide 6000 gauss on the sample.
- (16) Pump the medium chamber in order to drain liquid helium into it.
- (17) Watch the temperature digits on LTC-11 until it shows the system cooling to a lower temperature.
- (18) Run the program to record 8 modes data automatically.
- (19) Adjust the flow rate of liquid helium to prevent the temperature of the system from falling too rapidly.
- (20) Stop recording data when the temperature falls below 8 K.
- (21) Turn off the magnetic device and check if the contact is ohmic at low temperatures.

- (22) Turn on the magnetic device and adjust to 4000 gauss.
- (23) Restart "New Hall measurement" program again.
- (24) Input the file name and the parameters of waiting time and the switching time of the relay box in the program.
- (25) Start the temperature control system of the program, and input its parameters.
- (26) Turn off the helium flow slowly in order to raise the temperature of the system gradually until it is completely turned off.
- (27) The program will stop recording data automatically when the system is above the temperature which the user entered in step 25. (It is usually set to be 290 K)
- (28) Adjust the magnetic device to 2000 gauss.
- (29) Repeat the steps 16-20.
- (30) Turn off the magnetic device and then turn off the cooling water.
- (31) Repeat the steps 23-27.
- (32) Turn off the Keithley 2000, Keithley 224, LTC-11, and the computer.
- (33) The experiment is completed.

Chapter 4

Transport in $\text{Al}_x\text{Ga}_{1-x}\text{N}/\text{GaN}$

HEMTs with different Al compositions

4-1 Introduction

Recently, AlGa_xN/GaN heterostructures have been attracting much attention because of their potentials for high-temperature and high-power microwave electronic devices [1-6]. The electron effective mass in GaN is 0.22 m_e , which is about three times higher than that in GaAs. The low-field mobility of bulk GaN is therefore much smaller than that of GaAs. However, GaN has a larger peak electron velocity, larger saturation velocity, higher thermal stability, and a larger band gap, making it very suitable for use as channel-material in microwave power devices. Moreover, the outstanding performance of AlGa_xN/GaN heterostructures is due to the existence of a two-dimensional electron gas (2DEG) with carrier concentration of 10^{13} cm^{-2} or higher at the interface of AlGa_xN and GaN without intentionally doping, well in excess of those achievable in other III-V material systems.

The existence of the 2DEG at the interface of AlGa_xN and GaN without intentionally doping arises from the fact that there exist spontaneous polarization and piezoelectric polarization in AlGa_xN and GaN [6]. The spontaneous polarization results from the non-coincidence of the centers of cations and anions when they are in their lowest energy states; and the piezoelectric polarization is due to lattice mismatch strain and thermal strain caused by the difference in the thermal expansion coefficient of the AlGa_xN and GaN layers.

Because of the polarizations in AlGa_xN and GaN, sheet charges

accumulate at the AlGa_xN/GaN interface. If the sheet charges are positive, free electrons will compensate for them during the cooling process after growth.

The advantages of AlGa_xN/GaN heterostructures over the other III-V systems have led to a number of attempts to fabricate high electron mobility transistors from AlGa_xN/GaN heterostructures with various techniques. The first group to succeed employed metal organic chemical vapor deposition (MOCVD) in growing AlGa_xN/GaN heterostructures on sapphire substrates in 1992, with a mobility of 2626 cm²/Vs at low temperatures [7]. In 1995, the low-temperature mobility of the 2DEG in the AlGa_xN/GaN heterostructures was enhanced to 5000 cm²/Vs by using MOCVD on sapphire substrates [8], and it was further increased to 5700 cm²/Vs in 1996 due to the improvement of material quality [9].

By 1999, a low-temperature mobility as high as 11000 cm²/Vs has been attained on a SiC substrate with MOCVD [10]. This is attributed to the much smaller lattice mismatch (about 3.5%) and thermal mismatch (about 25%) between SiC and GaN [11], which results in GaN layers with improved microstructural, electrical, and optical properties. On the contrary, the lattice mismatch (about 16%) and thermal mismatch (about 34%) between GaN and sapphire could lead to a high density of threading dislocations in GaN [11]. However, sapphire is still the substrate of choice for growing AlGa_xN/GaN heterostructures because of its insulating property.

Hence, it is pertinent that the quality of AlGa_xN/GaN heterostructures grown on sapphire substrates is improved. Recently, AlGa_xN/AlN/GaN based on AlN/sapphire template substrates was grown by metal-organic vapor phase epitaxy (MOVPE) [6]. The mobility at room temperature is approximately 2100 cm²/Vs and at 15 K it is as high as around 25500 cm²/Vs, which is much higher than the values found in previous samples.

In this chapter, we will report measurements on Al_xGa_{1-x}N/GaN HEMTs grown on a sapphire substrate with different Al contents, and determine the Al fraction which will yield the highest mobility.

4-2 Experiment

We performed measurements on three samples in our study. All the samples were grown by MOVCD at Chang-Gung University run by Prof. C.-A. Chang, Prof. N. C. Chen and Prof. P. H. Chang. Figure 4-1 shows a schematic diagram of the $\text{Al}_x\text{Ga}_{1-x}\text{N}/\text{GaN}$ heterostructure. First, a thin LT-GaN was grown on a sapphire substrate as a nucleation layer, and it was followed by a layer of undoped GaN 1.5 μm in thickness. Lastly, a 30nm thick undoped $\text{Al}_x\text{Ga}_{1-x}\text{N}$ layer was grown on top, where x is 0.11, 0.15, and 0.25 respectively. The symbol “LT” denotes that the layer was grown at a lower temperature of 600°C, and the symbol “HT” denotes that the layer was grown at a higher temperature of 1100°C.

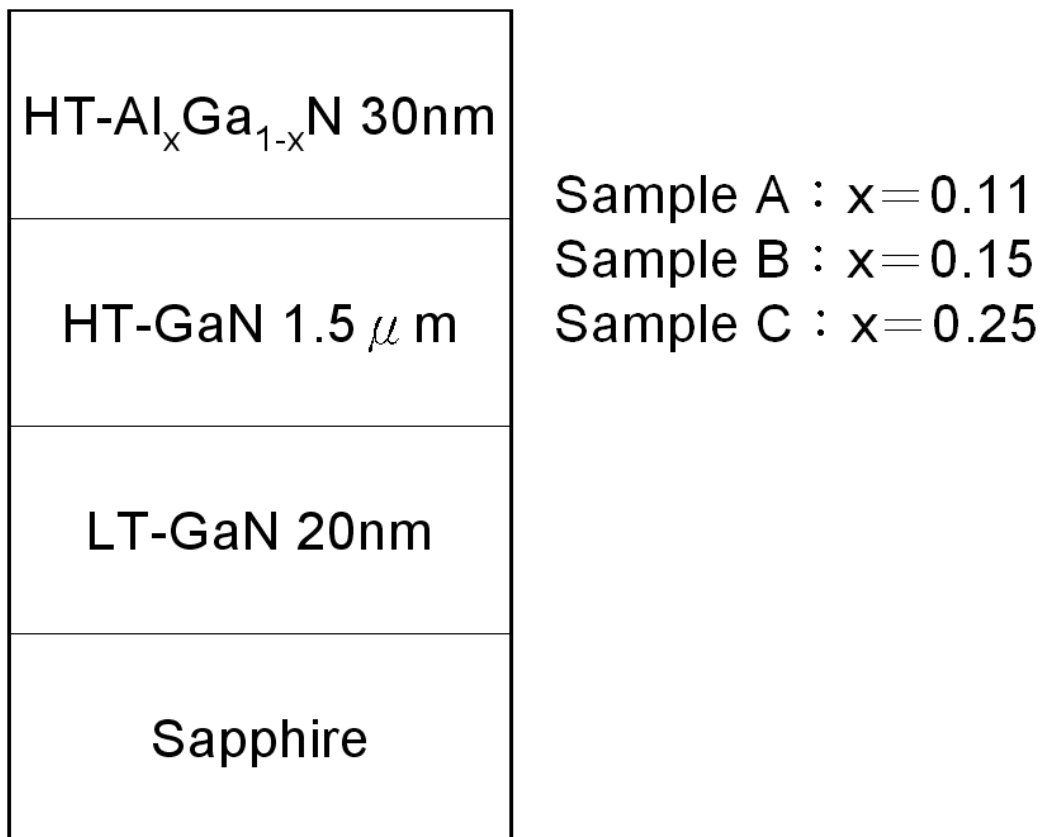


Figure 4-1. The schematic diagram of $\text{Al}_x\text{Ga}_{1-x}\text{N}/\text{GaN}$ heterostructure where x is 0.11, 0.15, and 0.25 respectively.

To ensure that the contacts will work at low temperatures, we first perform measurements on our samples in a closed cycle system. Figure 4-2 shows the R_{xx} result for the three samples. We can see that resistances

of all three samples fall with decreasing temperature and saturate at low temperatures. This implies that the two-dimensional electron gas may be behaving like a metal. At high temperatures, the electronic scattering is dominated by phonons. On the other hand, phonon scattering becomes negligible at low temperature, and imperfection scattering, which is temperature-independent, begins to dominate the electronic scattering. Therefore, the resistances of the samples will saturate at low temperatures.

After the measurements in the closed cycle system, we have successfully verified that the contacts do indeed work well at low temperatures. Thereafter, we proceed with the measurement of the three samples in the Hall effect system, and the results are shown below.

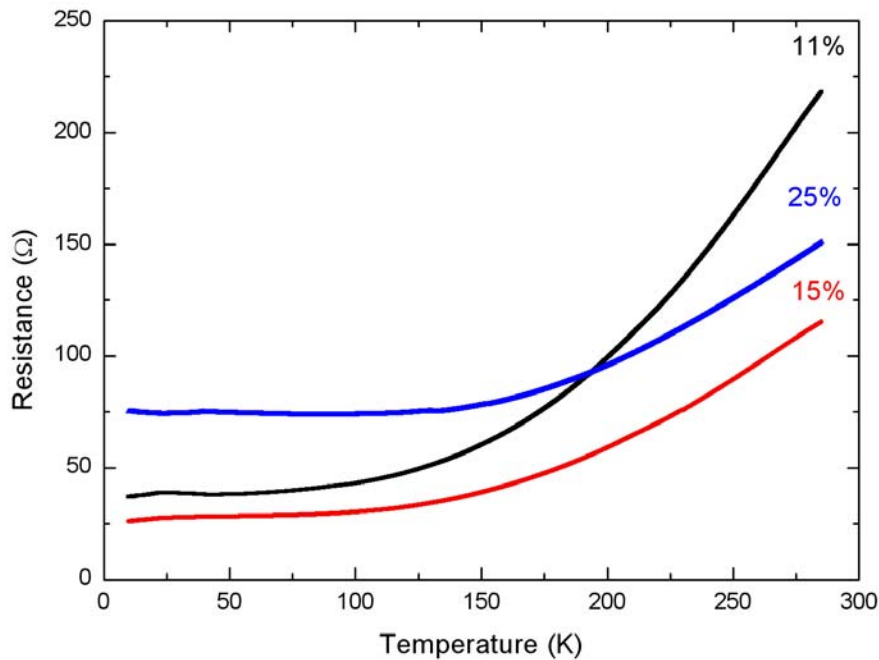


Figure 4-2. The resistance as a function of temperature measured in the close cycle system. The result implies that the two-dimensional electron gas behaves like a metal.

4-3 Results and discussions

First of all, we measured the resistivity of the three samples in the Hall system. Following van der Pauw's method [12-14], we can determine the sample resistivity by two R_{xx} measurements without having to take into account the shape and size of the sample. Figure 4-3 shows the resistivities of three samples as a function of temperature. We can see that the trend for the resistivities are similar to that for the resistances, namely, that the resistivities decrease as the temperature decreases and saturate at low temperatures due to imperfection scattering.

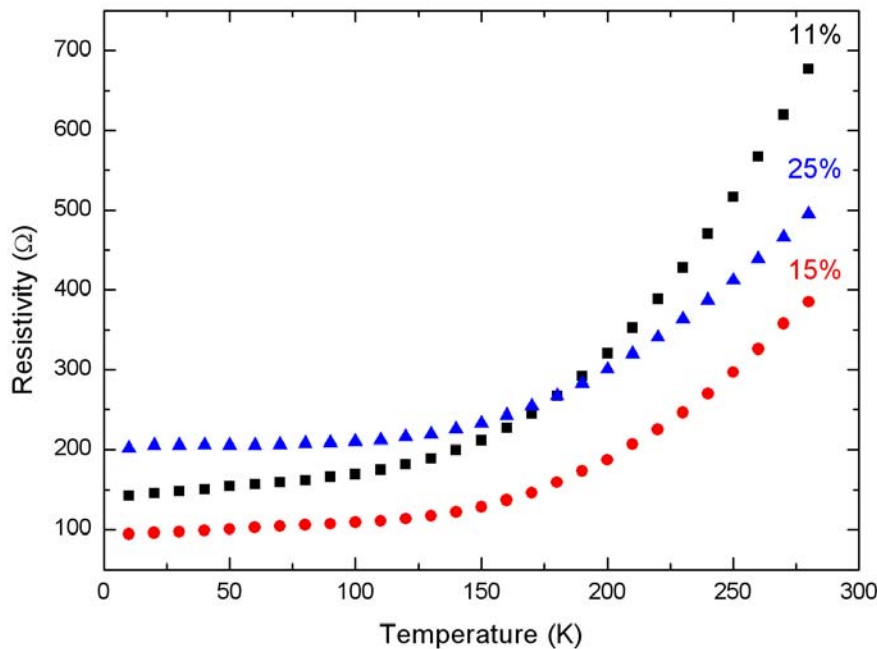


Figure 4-3. Resistivity as a function of temperature. This result strongly suggests that two-dimensional electron gas behaves like a metal.

The next physical quantity we measured in this Hall system was the carrier concentration. Figure 4-4 shows the variation of the carrier concentration with different Al fraction. We can see that as the Al fraction in $\text{Al}_x\text{Ga}_{1-x}\text{N}/\text{GaN}$ heterostructures increases, so does the 2DEG concentration. This result can be explained by the fact that when the Al fraction increases, the polarization in $\text{Al}_x\text{Ga}_{1-x}\text{N}$ would increase

correspondingly, inducing more sheet charges at the interface of $\text{Al}_x\text{Ga}_{1-x}\text{N}$ and GaN. Therefore, for an $\text{Al}_x\text{Ga}_{1-x}\text{N}/\text{GaN}$ heterostructure with a higher Al composition, more electrons would be attracted to compensate for the sheet charges near the $\text{Al}_x\text{Ga}_{1-x}\text{N}/\text{GaN}$ interface. The result is that the 2DEG concentration would be higher for an $\text{Al}_x\text{Ga}_{1-x}\text{N}/\text{GaN}$ sample with a higher Al composition.

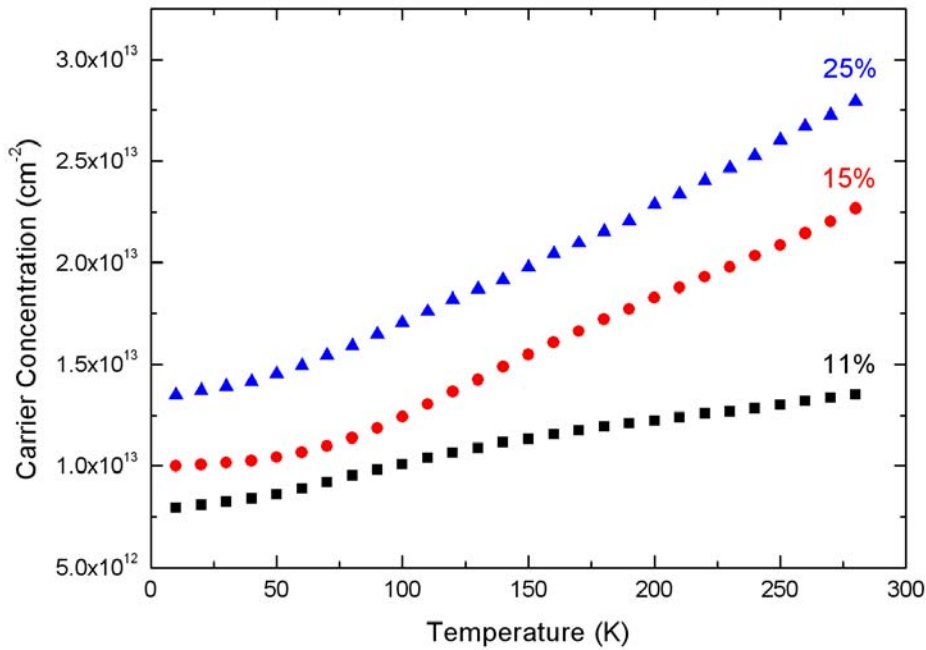


Figure 4-4. Two-dimensional carrier concentration as a function of temperature. We can see that the carrier concentration will increase with the increasing Al fraction in $\text{Al}_x\text{Ga}_{1-x}\text{N}$.

In addition to the experimental measurements, we can calculate quantitatively the 2DEG concentrations at the interface of $\text{Al}_x\text{Ga}_{1-x}\text{N}$ and GaN with the respect to Al composition in $\text{Al}_x\text{Ga}_{1-x}\text{N}$. According to section 4 in chapter 1, the reason for the existence of the 2DEG in $\text{Al}_x\text{Ga}_{1-x}\text{N}/\text{GaN}$ heterostructures is the polarizations of $\text{Al}_x\text{Ga}_{1-x}\text{N}$ and GaN as shown in figure 1-9 [6]. The differences in polarization between $\text{Al}_x\text{Ga}_{1-x}\text{N}$ and GaN at the interface will produce sheet charges, and electrons will be attracted

to the triangular well by the sheet charges. According to Eq. 1-12, we have

$$\sigma = (P_{SP} + P_{PE})_{AlGaN} - (P_{SP})_{GaN}. \quad (4-1)$$

We can also use interpolation to estimate the spontaneous polarization of $Al_xGa_{1-x}N$ by AlN and GaN [6]. Our estimate of the spontaneous polarization of $Al_xGa_{1-x}N$ is

$$P_{SP}(x) = (-0.029 - 0.052 x) \text{ C/m}^2. \quad (4-2)$$

Next, we can write down the piezoelectric polarization of $Al_xGa_{1-x}N$ in terms of the piezoelectric coefficients e_{33} and e_{13} :

$$P_{PE} = e_{33} \varepsilon_z + e_{31} (\varepsilon_x + \varepsilon_y), \quad (4-3)$$

where

$$\varepsilon_z = \frac{c - c_0}{c_0}, \quad (4-4)$$

$$\varepsilon_x = \varepsilon_y = \frac{a - a_0}{a_0}, \quad (4-5)$$

and a_0 and c_0 are the equilibrium values of the lattice parameters. The relation between the lattice constants is

$$\frac{c - c_0}{c_0} = -2 \frac{C_{13}}{C_{33}} \frac{a - a_0}{a_0}, \quad (4-6)$$

where C_{13} and C_{33} are the elastic constants. Likewise, we can use interpolation to estimate the values of a , C_{13} , C_{33} , e_{31} , and e_{33} [6, 15, 16].

$$a(x) = (3.189 - 0.077 x) \times 10^{-10} \text{ m}, \quad (4-7)$$

$$C_{13}(x) = (103 + 5 x) \text{ Gpa}, \quad (4-8)$$

$$C_{33}(x) = (405 - 32 x) \text{ Gpa}, \quad (4-9)$$

$$\varepsilon_{31}(x) = (-0.49 - 0.11 x) \text{ C/m}^2, \quad (4-10)$$

$$\varepsilon_{33}(x) = (0.73 + 0.73 x) \text{ C/m}^2. \quad (4-11)$$

Combining equations 4-1 to 4-11, we can calculate the sheet charge density. Subsequently, we can compute the 2DEG concentration at the

interface of $\text{Al}_x\text{Ga}_{1-x}\text{N}$ and GaN with respect to Al composition:

$$n(x) = \frac{\sigma(x)}{e} - \left(\frac{\varepsilon_0 \varepsilon(x)}{d e^2}\right) [e\Phi_b(x) + E_F(x) - \Delta E_C(x)], \quad (4-12)$$

where d is the width of the $\text{Al}_x\text{Ga}_{1-x}\text{N}$, ε is the dielectric constant, $e\Phi_b$ is the Schottky barrier, E_F is the Fermi level with respect to the GaN conduction-band-edge energy, and ΔE_C is the conduction band offset at the $\text{Al}_x\text{Ga}_{1-x}\text{N}$ /GaN interface. Again, we can estimate ε , $e\Phi_b$, E_F , and ΔE_C from the followings [17-23]:

$$\varepsilon(x) = 9.5 - 0.5 x, \quad (4-13)$$

$$e\Phi_b(x) = (0.84 + 1.3 x) \text{ eV}, \quad (4-14)$$

$$E_F(x) = E_0(x) + \frac{\pi\hbar^2}{m^*} n, \quad (4-15)$$

where E_0 is the ground subband level of the 2DEG,

$$E_0(x) = \left\{ \frac{9\pi\hbar e^2}{8\varepsilon_0 \sqrt{8m^*}} \frac{n(x)}{\varepsilon(x)} \right\}^{2/3}, \quad (4-16)$$

and m^* is the effective electron mass, which is about $0.22 m_e$,

$$\Delta E_C(x) = 0.7 [E_g(x) - E_g(0)], \quad (4-17)$$

Here E_g is the band gap of $\text{Al}_x\text{Ga}_{1-x}\text{N}$ and is measured to be

$$E_g(x) = x E_g(\text{AlN}) + (1 - x) E_g(\text{GaN}) - x(1 - x) 1.0 \text{ eV}, \quad (4-18)$$

with $E_g(\text{AlN})=6.13 \text{ eV}$ and $E_g(\text{GaN})=3.42 \text{ eV}$.

Substituting Eq. 4-13 to Eq. 4-18 into Eq. 4-12, we obtain an equation for $n(x)$. Solving this equation by the alternative iteration method, we can accurately determine the 2DEG concentration at the interface of $\text{Al}_x\text{Ga}_{1-x}\text{N}$ and GaN with respect to the Al composition. Figure 4-5 shows the theoretical calculations of the 2DEG concentration as a function of the Al content, and we compare them with the experimental data. In figure 4-5, the solid line represents the results of the theoretical calculation and the

spots represent the 2DEG concentrations measured experimentally. We can see that the experimental values match the theoretical calculations very closely. This affirms our previous discussion on the 2DEG concentration, namely, that the 2DEG concentration increases with increasing Al composition in $\text{Al}_x\text{Ga}_{1-x}\text{N}$.

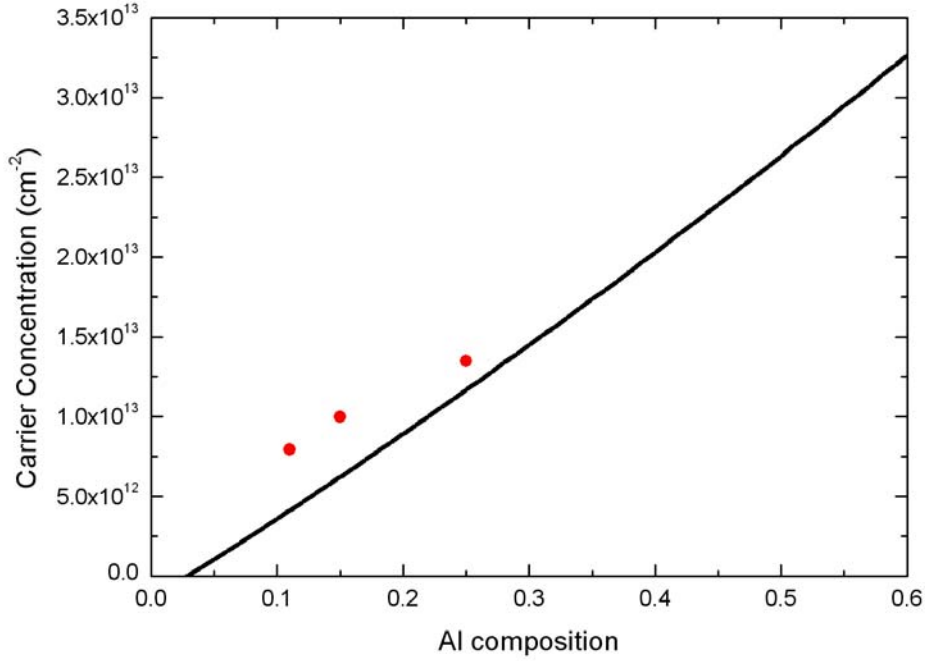


Figure 4-5. Carrier concentration as a function of Al composition. The solid line represents the theoretical calculation, and the spots represent the experimental measurements at 10 K.

In order to gain further understanding of the transport properties of our three samples, we have measured their mobilities. In chapter 2, we introduced the concept that mobility is proportional to the mean free time of electrons in the sample. From Eq. 2-19, we have

$$\mu \equiv \frac{|\mathbf{v}_d|}{|\mathbf{E}|} = \frac{\frac{J}{ne}}{\rho J} = \frac{1}{ne\rho}. \quad (4-19)$$

By substituting the carrier concentration and resistivity at various

temperatures, we obtain the mobility of the samples as a function of temperature, as shown in figure 4-6.

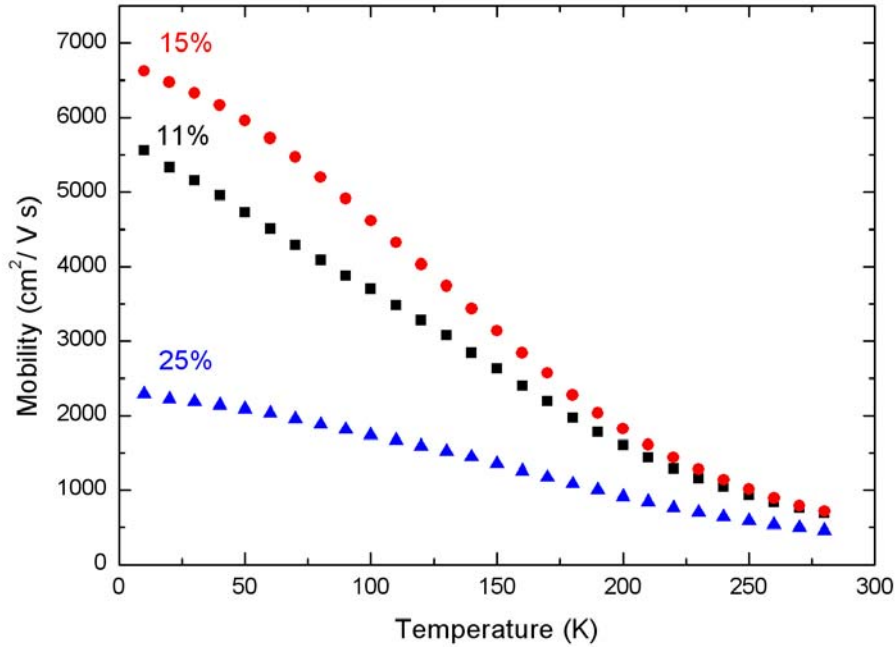


Figure 4-6. Mobility as a function of temperature.

From figure 4-6, we find that the mobilities of the three samples are similar at room temperature. This is because the electron mobility is limited by polar optical scattering near room temperature [24]. At low temperatures, the mobility is largely dependent on deformation potential and piezoelectric scattering. These effects introduce a $1/T$ dependence on the mobility [25]. Figure 4-7 shows the mobilities of the three samples with respect to $1/T$. We can see that at high temperatures, the mobilities of all three samples are almost linear in $1/T$. This is consistent with the previous assertion that polar optical phonon dominates the mobility at room temperature.

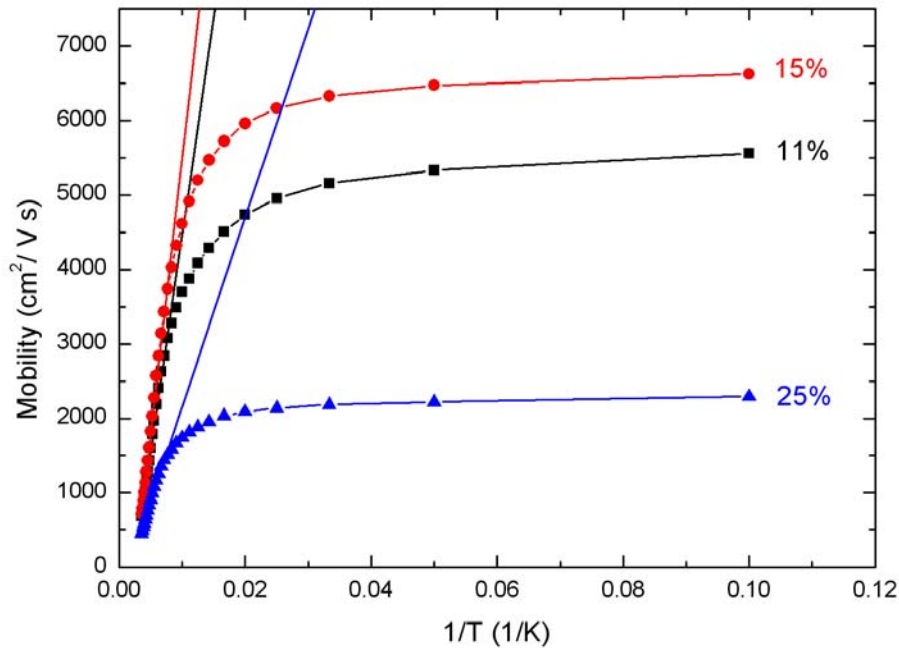


Figure 4-7. Mobility as a function of $1/T$. We can clearly see the linear dependence at room temperature.

Next, figure 4-8 shows the 2DEG mobility as a function of the Al content. We see that as the Al content increases from 11% to 15%, the 2DEG mobility increases. However, as Al content increases further to 25%, the 2DEG mobility drops abruptly. There are two possible explanations for the abrupt reduction of the electron mobility at $x > 0.15$. Firstly, as can be seen from figure 4-5, the 2DEG concentration increases as the Al content increases. Conversely, as the Al content increases, the 2DEG concentration will increase as well. When the ground subband states are all occupied, the remaining electrons will occupy the higher subbands in the GaN quantum wells. The occupation of multiple subbands would result in a reduction of the electron mobility due to intersubband scattering. Secondly, the lattice mismatch between $\text{Al}_x\text{Ga}_{1-x}\text{N}$ and GaN increases with increasing Al content [26]. Therefore, there would be more strains between $\text{Al}_x\text{Ga}_{1-x}\text{N}$ and GaN. The increased strains may lead to increased roughness, which reduces the 2DEG mobility.

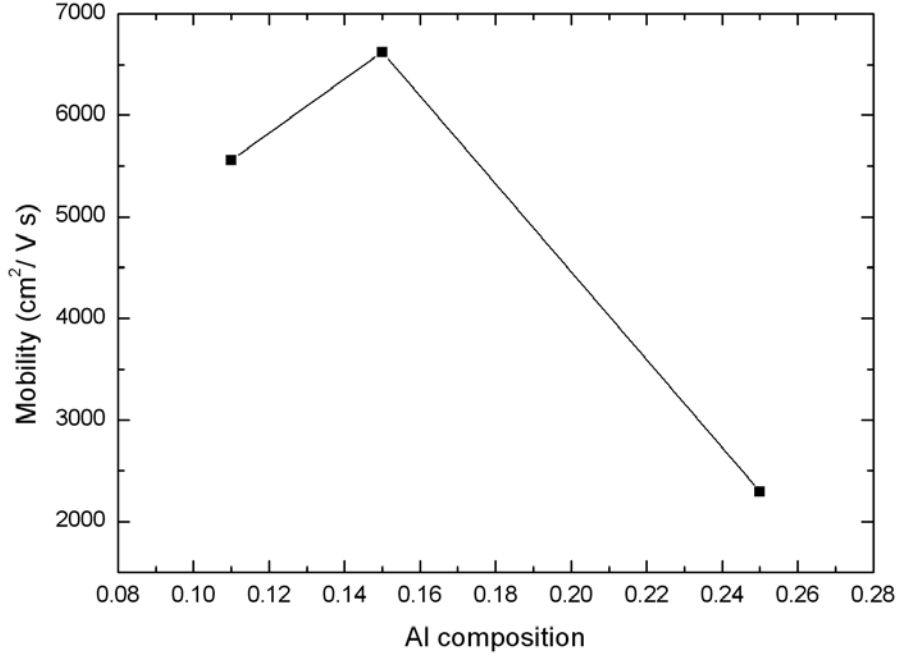


Figure 4-8. 2DEG mobility at 10 K as a function of Al composition.

Lastly, we measured the activation energy of the 2DEG. From Ref. [27], we have a simple equation from which we can obtain the activation energy of the 2DEG at the $\text{Al}_x\text{Ga}_{1-x}\text{N}/\text{GaN}$ interface, that is

$$n \propto e^{-\frac{E_d}{2k_B T}}, \quad (4-20)$$

where E_d is the activation energy [27-30]. For convenience, we can rewrite Eq. 4-20 as

$$\text{Log } n = -(\text{Log } e) \frac{E_d}{2000 k_B} \frac{1000}{T} + \text{Constant}. \quad (4-21)$$

We can next redraw figure 4-4 in the same manner as figures 4-9, 4-10, and 4-11. From these figures, we can deduce the activation energy. Our results show that the activation energies of the three samples with 11%, 15%, and 25% Al contents are 10.8, 23.7, and 25.9 meV respectively. It appears that the activation energy increases with increasing Al composition in $\text{Al}_x\text{Ga}_{1-x}\text{N}$. We speculate that this could be related to the increasing lattice mismatch between $\text{Al}_x\text{Ga}_{1-x}\text{N}$ and GaN. As the Al composition in $\text{Al}_x\text{Ga}_{1-x}\text{N}$ increases, the lattice mismatch between

$\text{Al}_x\text{Ga}_{1-x}\text{N}$ and GaN increases. This increased lattice mismatch could result in a larger defect density. Therefore a higher activation energy is required to thermally activate the carriers into the 2DEG region.

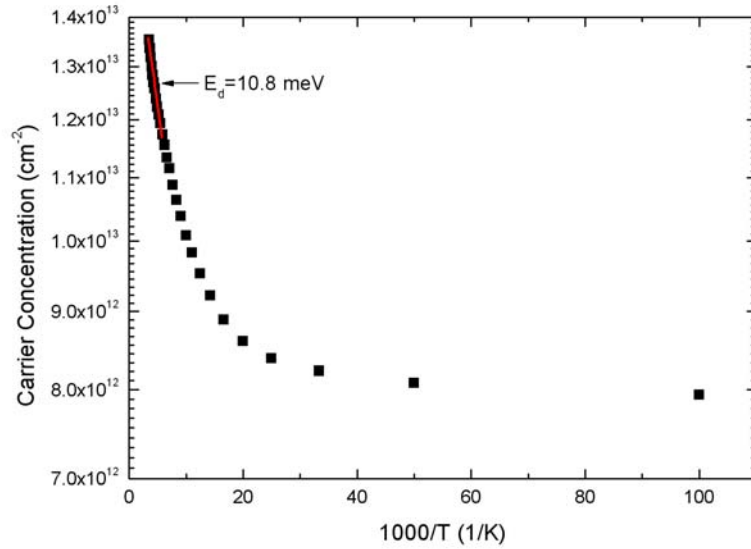


Figure 4-9. Sample A: The logarithm of carrier concentration with respect to 1000 times the reciprocal of temperature. The activation energy is measured to be 10.8 meV.

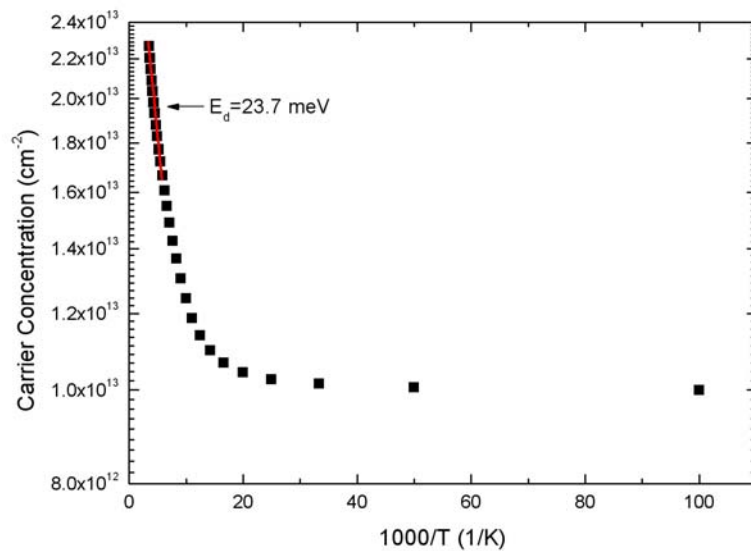


Figure 4-10. Sample B: The logarithm of carrier concentration with respect to 1000 times the reciprocal of temperature. The activation energy is measured to be 23.7 meV.

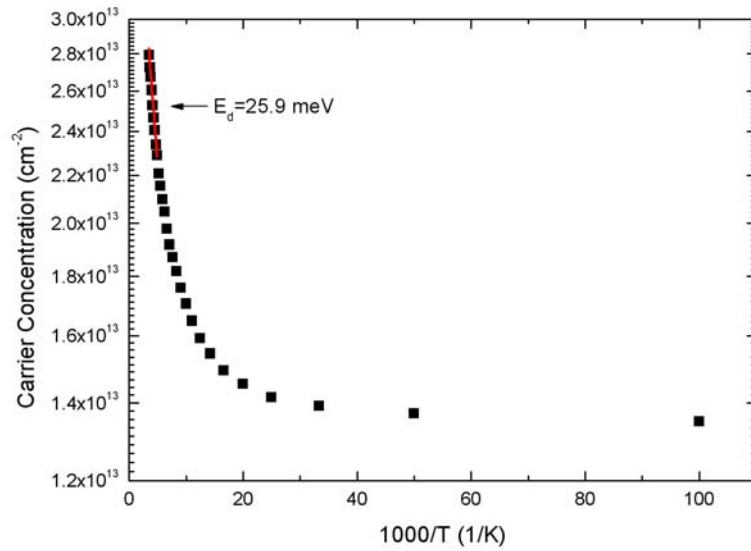


Figure 4-11. Sample C: The logarithm of carrier concentration with respect to 1000 times the reciprocal of temperature. The activation energy is measured to be 25.9 meV.

4-4 Summary

In this chapter, we have presented measurements on $\text{Al}_x\text{Ga}_{1-x}\text{N}/\text{GaN}$ HEMTs with different Al contents. First of all, we showed that the resistivity of the 2DEG system behaves like that of a metal, which decreases as the temperature decreases due to electron-phonon scattering and saturates at low temperatures due to impurity scattering.

In addition, we measured the carrier concentration of $\text{Al}_x\text{Ga}_{1-x}\text{N}/\text{GaN}$ HEMTs and found that the 2DEG concentration increases with increasing Al content. This result can be explained by the fact that when the Al fraction increases, the polarization in $\text{Al}_x\text{Ga}_{1-x}\text{N}$ would increase correspondingly, inducing more sheet charges at the interface of $\text{Al}_x\text{Ga}_{1-x}\text{N}$ and GaN. Therefore, for an $\text{Al}_x\text{Ga}_{1-x}\text{N}/\text{GaN}$ heterostructure with a higher Al composition, more electrons would be attracted to compensate for the sheet charges near the $\text{Al}_x\text{Ga}_{1-x}\text{N}/\text{GaN}$ interface. The result is that the 2DEG concentration would be higher for an $\text{Al}_x\text{Ga}_{1-x}\text{N}/\text{GaN}$ sample with a higher Al composition. In addition, we calculated the 2DEG concentration quantitatively with respect to the Al content, and also found

that the experimental values matched the theoretical calculations very closely. This is consistent with our previous discussion.

Next, we measured the 2DEG mobility and found that the mobilities at room temperature are almost the same and linear in $1/T$. This is consistent with the fact that electron-phonon scattering dominates the mobility at high temperatures. Additionally, we find that 2DEG mobility increases as the Al content increases from 11% to 15%, but falls abruptly at 25%. There are two possible reasons for this. The first is that electron density at the Al content of 25% is so high that electrons fill up all the ground subband states. Hence the residual electrons could start to occupy the second subband in the GaN quantum well. This occupation of multiple subbands would result in intersubband scattering and thus reduce the 2DEG mobility. The second reason is that the lattice mismatch between $\text{Al}_x\text{Ga}_{1-x}\text{N}$ and GaN increases with increasing Al content. The larger lattice mismatch will introduce more strains between $\text{Al}_x\text{Ga}_{1-x}\text{N}$ and GaN, and thus increase the roughness, which in turn reduce the 2DEG mobility.

Lastly, we measured the activation energy of $\text{Al}_x\text{Ga}_{1-x}\text{N}/\text{GaN}$ HEMTs. Our result indicates that the activation energy increases with increasing Al content. As the Al content increases, the lattice mismatch between $\text{Al}_x\text{Ga}_{1-x}\text{N}$ and GaN becomes more prominent. This increased lattice mismatch could induce a larger defect density. Therefore a higher activation energy is required to thermally activate the carriers into the 2DEG region.

From the above investigation of $\text{Al}_x\text{Ga}_{1-x}\text{N}/\text{GaN}$ HEMTs with different Al contents, we see that $\text{Al}_x\text{Ga}_{1-x}\text{N}/\text{GaN}$ HEMTs with 15% Al content would have the highest mobility among the three. Therefore, in the next chapter, we will investigate samples on, however, p-type silicon substrates with 15% of Al content. The aim is to fabricate high-mobility $\text{Al}_x\text{Ga}_{1-x}\text{N}/\text{GaN}$ HEMTs on silicon substrate. This is an interesting project as it may pave way to an experimental realization of $\text{Al}_x\text{Ga}_{1-x}\text{N}/\text{GaN}$ HEMTs compatible with the very mature Si technology.

References

1. L. F. Eastman, V. Tilak, J. Smart, B. M. Green, E. M. Chumbes, R. Dimitrov, H. Kim, O. S. Ambacher, N. Weimann, T. Prunty, M. Murphy, W. J. Schaff, and J. R. Shealy, *IEEE Trans. Electron Devices* **48**, 479 (2001).
2. U. K. Mishra and Y.-F. Wu, *IEEE Trans. Microwave Theory Tech.* **46**, 756 (1998).
3. Y.-F. Wu, J. P. Ibbetson, P. Parikh, B. P. Keller, U. K. Mishra, and D. Kapolnek, *IEEE Trans. Electron Devices* **48**, 586 (2001).
4. T. Egawa, G. Y. Zhao, H. Ishikawa, M. Umeno, and T. Jimbo, *IEEE Trans. Electron Devices* **48**, 603 (2001).
5. M. Miyoshi, H. Ishikawa, T. Egawa, K. Asai, M. Mouri, T. Shibata, M. Tanaka, and O. Oda, *Appl. Phys. Lett.* **85**, 1710 (2004).
6. O. Ambacher, J. Smart, J. R. Shealy, N. G. Weimann, K. Chu, M. Murphy, W. J. Schaff, and L. F. Eastman, *J. Appl. Phys.* **85**, 3222 (1999).
7. M. A. Khan, J. N. Kuznia, J. M. Van Hove, N. Pan, and J. Carter, *Appl. Phys. Lett.* **60**, 3027 (1992).
8. M. A. Khan, Q. Chen, C. J. Sun, M. Shur, and B. Gelmont, *Appl. Phys. Lett.* **67**, 1429 (1995).
9. J. M. Redwing, M. A. Tischler, J. S. Flynn, S. Elhamri, M. Ahoujja, R. S. Newrock, W. C. Mitchel, and W. Mitchel, *Appl. Phys. Lett.* **69**, 963 (1996).
10. R. Gaska, M. S. Shur, A. D. Bykhovski, A. O. Orlov, and G. L. Sneider, *Appl. Phys. Lett.* **74**, 287 (1999).
11. A. Krost and A. Dadgar, *Phys. Stat. Sol. (a)* **194**, 361 (2002).
12. L. J. Van der Pauw, *Philips Research Report No.* **13**, 1 (1958).
13. Daniel W. Koon, *Rev. Sci. Instrum.* **60**, 271 (1989).
14. Daniel W. Koon, Arshad A. Bahl, and Edward O. Duncan, *Rev. Sci. Instrum.* **60**, 275 (1989).
15. A. F. Wright, *J. Appl. Phys.* **82**, 2833 (1997).
16. F. Bernardini, V. Fiorentini, and D. Vanderbilt, *Phys. Rev. B* **56**, 10024 (1997).
17. K. Tsubouchi, N. Miskoshiba, *IEEE Trans. Sonics Ultrason.* **SU-32**, 634 (1985).
18. A. S. Barker Jr. and M. Ilegems, *Phys. Rev. B* **7**, 743 (1973).

- 19.L. S. Yu, D. J. Qiao, Q. J. Xing, S. S. Lau, K. S. Boutros, and J. M. Redwing, *Appl. Phys. Lett.* **73**, 238 (1998).
- 20.M. S. Shur, *Mater. Res. Soc. Symp. Proc.* **483**, 15 (1998).
- 21.G. Martin, S. Strite, A. Botchkarev, A. Agarwal, A. Rockett, H. Morkoc, W. R. L. Lambrecht, and B. Segall, *Appl. Phys. Lett.* **65**, 610 (1994).
- 22.G. Martin, A. Botchkarev, A. Rockett, and H. Morkoc, *Appl. Phys. Lett.* **68**, 2541 (1996).
- 23.D. Brunner, H. Angerer, E. Bustarret, R. Höpler, R. Dimitrov, O. Ambacher, and M. Stutzmann, *J. Appl. Phys.* **82**, 5090 (1997).
- 24.W. Walukiewicz, H. E. Ruda, J. Lagowski, and H. C. Gatos, *Phys. Rev. B* **30**, 4571 (1984).
- 25.Loren Pfeiffer, K. W. West, H. L. Stormer, and K. W. Baldwin, *Appl. Phys. Lett.* **55**, 1888 (1989).
- 26.L. Hsu and W. Walukiewicz, *J. Appl. Phys.* **89**, 1783 (2001).
- 27.P. M. Mooney, *J. Appl. Phys.* **67**, 1 (1990).
- 28.Ikai Lo, S. J. Chen, Y. C. Lee, and Li-Wei Tu, W. C. Mitchel, M. Ahoujja, R. E. Perrin, R. C. Tu, Y. K. Su, W. H. Lan, and S. L. Tu, *Phys. Rev. B* **57**, 6819 (1998).
- 29.Ikai Lo, K. Y. Hsieh, S. L. Hwang, Li-Wei Tu, W. C. Mitchel and A. W. Saxler, *Appl. Phys. Letts.* **74**, 2167 (1999).
- 30.Naresh Chand, Tim Henderson, John Klem, W. Ted Masselink, Russ Fischer, Yia-Chung Chang, and Hadis Morkoc, *Phys. Rev. B* **30**, 4481 (1984).

Chapter 5

Measurements of AlGaN/GaN HEMTs grown on p-type silicon substrates

5-1 Introduction

AlGaN/GaN high electron mobility transistors (HEMTs) have been extensively studied for their applications in high-power high-temperature microwave devices [1-3], in high-frequency field effect transistors, and in blue light-emitting and laser diodes [4]. In most cases, AlGaN/GaN HEMTs were grown on sapphire substrates because of the smaller lattice mismatch (about 16%) and thermal mismatch (about 34%) between GaN and sapphire [5]. However, Si can be regarded as an alternative to commercial sapphire substrates for nitride-based devices due to its low cost and large wafer size.

Despite these advantages, silicon has not been popular as a substrate material for GaN growth due to several problems. The most serious drawback is development of cracks in the GaN film due to the stress between GaN and silicon substrates. The magnitudes of these stresses do not pose a problem for sapphire substrates, but they can be significant in silicon substrates. Such noticeable stresses between GaN and the silicon substrates result from the large lattice mismatch (about 17%) and thermal mismatch (about 54%) between GaN and silicon substrates [5-8].

In 1971, group III nitrides had already been deposited on Si via metal organic chemical vapor phase epitaxy (MOVPE) by Manasevit and co-workers, who grew AlN layers on Si (111) [9]. Other than these breakthroughs, progresses in the next fifteen to twenty years were few and

far between. In the late 90s, a lot of attention was raised when the first LED structures grown by molecular beam epitaxy (MBE) demonstrated that p-type doping of GaN on Si (and thus various devices) is achievable [10, 11].

However, the performances of GaN on Si remained poor when compared to GaN on sapphire, with X-ray rocking curve full widths at half maximum (FWHM) for the GaN (0002) reflection at around 1000 arcsec, which is three to five times broader than the average layers on sapphire. In addition, there is also a broad photoluminescence (PL). Subsequently, a lot of efforts were devoted to improve the layer quality grown not only on sapphire but also on Si.

In this chapter, we present our measurements of AlGaIn/GaN HEMTs grown by MOVPE on Si substrates using AlN as an intermediate layer. The samples were all grown by the group of Profs. C.-A. Chang, N. C. Chen and P. H. Chang at Chang-Gung University. The motivation for this work is that recent experiments show that by inserting a thin Si₅N₄ film before growing GaN on Si substrates, the stresses between GaN and silicon substrates can be greatly reduced [12]. Hence, we deposited a thin Si₅N₄ layer for 0, 5, and 10 seconds in our samples respectively, and investigated the electrical properties of the samples with different Si₅N₄ deposition time.

5-2 Experiment

Figure 5-1 shows the schematic diagram of the three samples measured in this work. They were all grown on silicon substrates by MOVPE. First of all, on account of the large lattice mismatch (about 17%) and thermal mismatch (about 54%) between Si and GaN, a few AlN layers were grown as intermediate layers between Si and GaN [13]. The symbol “LT” denotes that the layer was grown at a lower temperature of 600°C, and the symbol “HT” denotes that the layer was grown at a higher temperature of 1100°C. These AlN layers are grown to reduce the thermal strain between GaN and silicon substrates.

Furthermore, following to Ref. [12], we can insert a thin Si₅N₄ film after AlN layers were grown. This thin film will reduce the stress on GaN.

In this work, we grow three samples with 0, 5, and 10 seconds of Si₅N₄ deposition respectively. By comparing their electrical properties, we can understand the effect of the Si₅N₄ thin film on AlGa_xN/GaN HEMTs grown on silicon substrates.

Al _{0.15} Ga _{0.85} N	30nm	Sample D : x=0
Ud-GaN	400nm	Sample E : x=5
HT-AIN	12nm	Sample F : x=10
LT-AIN	12nm	
Ud-GaN	350nm	
Thin-Film Si ₅ N ₄	x seconds	
HT-AIN	25nm	
LT-AIN	25nm	
p – type Si substrate		

Figure 5-1. The schematic diagram of Al_{0.15}Ga_{0.85}N/GaN heterostructure, where x is 0, 5, 10 respectively.

Likewise, to ensure that the contacts will work at low temperatures, we first measure our samples in the close cycle system. Figure 5-2 shows the R_{xx} result for the three samples. Once again, the result shows that our 2DEG behavior is similar to that of a metal. At high temperatures, phonons dominate the electronic scattering, and therefore resistances decrease with decreasing temperature. At low temperatures, phonon scattering is negligible, and imperfection scattering, which is temperature-independent, dominates the electronic scattering. Therefore, resistances of these samples will saturate at low temperatures.

After measuring our samples in the close cycle system, we can be sure that our contacts do indeed work well at low temperatures. Consequently, we could now measure our samples in the Hall system. The results will be reported in the next section, which include the measurements on the resistivity, carrier concentration, and mobility of the three samples.

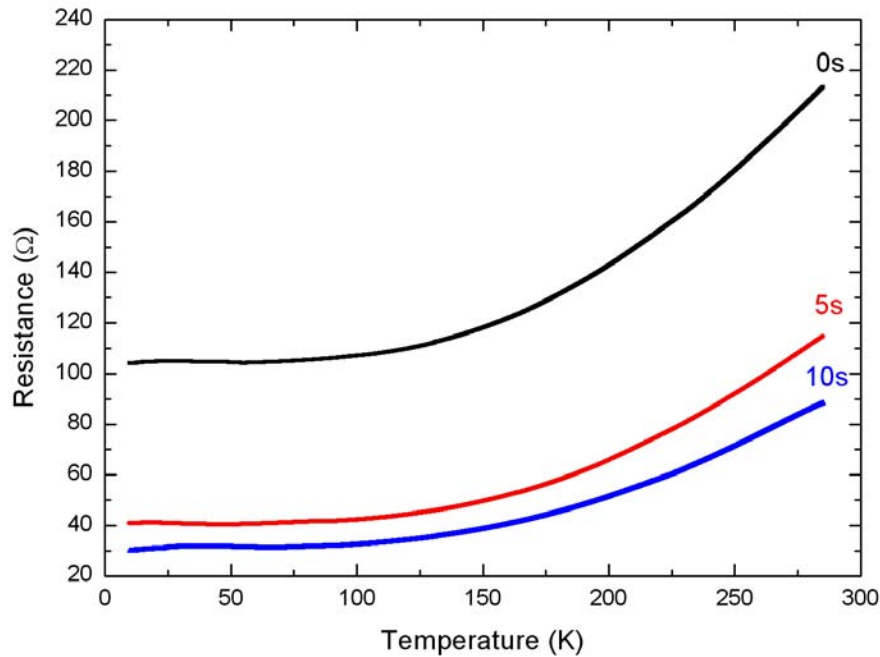


Figure 5-2. The resistance as a function of temperature measured in the close cycle system. The result implies that the two-dimensional electron gas behaves like a metal.

5-3 Results and discussions

The following measurements were performed in the Hall system. First of all, following van der Pauw's theory [14-16], we could easily determine the resistivity of a sample by two different-directional R_{xx} measurements. The resistivity is a more useful quantity than the resistance because it is an intrinsic property of the sample and independent of its shape. Figure 5-3 shows the resistivity of the three samples from room

temperature to low temperatures. The behavior of the resistivity is similar to that of a metal, where it increases rapidly at high temperatures and tends to saturate at low temperatures. In addition, we found that the resistivity was greatly reduced by a factor of about three times after we deposited the Si_5N_4 for either 5 seconds or 10 seconds. This shows that growing a Si_5N_4 thin film could greatly enhance the transport properties of the electrons in the 2DEG systems of AlGaIn/GaN HEMTs.

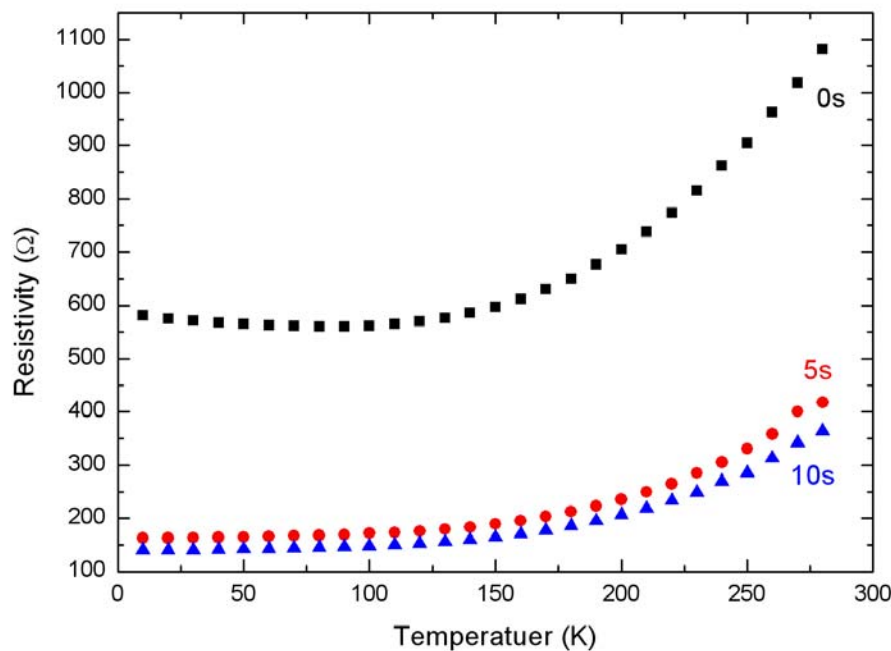


Figure 5-3. Resistivity as a function of temperature. We can see that the resistivity of samples with Si_5N_4 thin film was greatly reduced.

Next, we present our measurements of the carrier concentration in the Hall system. Figure 5-4 shows the variation of the carrier concentrations of the three samples as a function of temperature. We can see that within experimental errors, the carrier concentrations exhibit very little variation (about 15%, 7.4%, and 9.8% for sample D, E, and F respectively) over a wide range of temperature ($10 \text{ K} \leq T \leq 280 \text{ K}$). This demonstrates the formation of a 2DEG in our system even at room temperature.

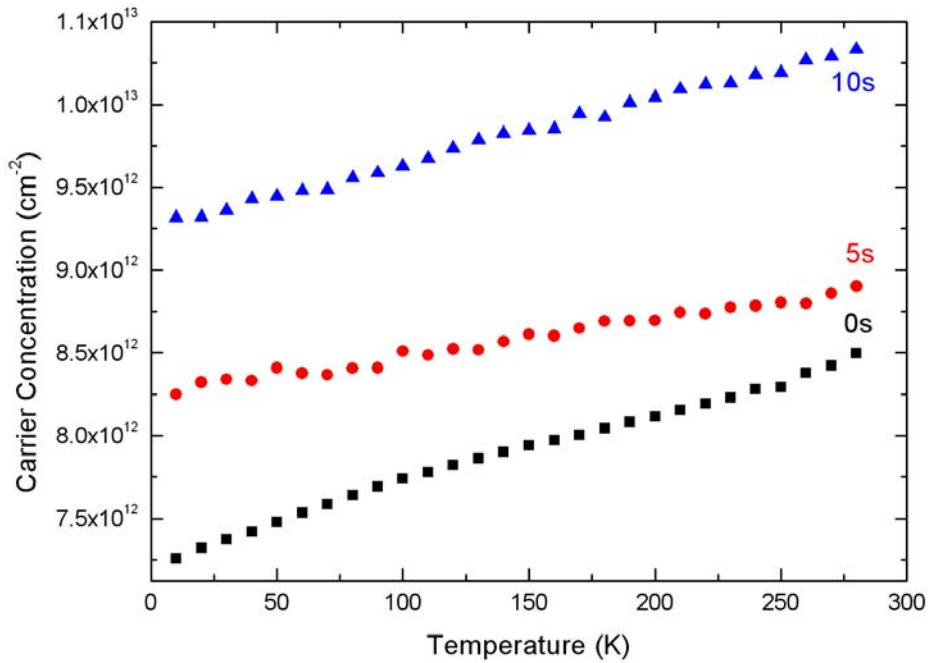


Figure 5-4. The carrier concentration as a function of temperature.

After the measurements on the carrier concentration and resistivity, we could calculate the mobility of the three samples from Eq. 4-19. Figure 5-5 shows the mobility of the samples as a function of temperature. We can see that the mobility decreases with increasing temperature. This is consistent with the fact that electron-phonon scattering increases with increasing temperature. We see that the quality of the sample is greatly enhanced after a Si_5N_4 thin film was grown. The mobility of sample E and sample F at 10 K is almost three times higher than that of sample D. This results from the stress reduction in GaN. The smaller the stress in GaN, the better the quality of GaN. Therefore, higher quality GaN will help in the formation of 2DEG in AlGaN/GaN HEMTs.

It should be pointed out that the mobility of sample F at low temperatures is slightly higher than that of sample E. However, their mobilities are almost identical at $T > 150$ K. This shows that the effect of the Si_5N_4 thin film saturates when we deposit Si_5N_4 for 5 seconds. There will not be any significant improvement in the mobility even if we deposit the Si_5N_4 for a period of time longer than 5 seconds.

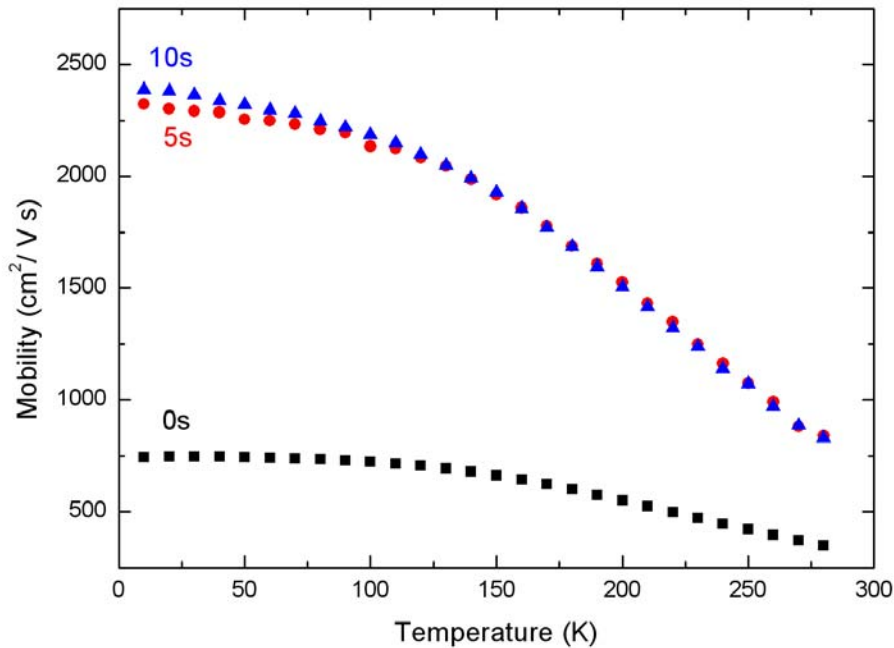


Figure 5-5. Mobility as a function of temperature. We can see that the mobility was greatly enhanced by about three times after we deposited a Si_3N_4 thin film in the sample.

However, similar measurements in chapter 4 show that the mobility of AlGaIn/GaN HEMTs with 15% Al content and grown on sapphire substrates is $6600 \text{ cm}^2/\text{Vs}$. Such a high mobility is way beyond anything we have attained in this chapter despite the fact that we have inserted a thin Si_3N_4 film precisely to enhance the mobility. Consequently, we conclude that it is very difficult to grow AlGaIn/GaN HEMTs on silicon substrates, which have mobilities as high as those grown on sapphire substrates. However, the Si_3N_4 treatment provides a practical way to achieve this goal.

In addition, we can redraw figure 5-5 as we did in chapter 4 (plotting the mobility with respect to $1/T$). Figure 5-6 shows the mobility with respect to $1/T$. As we have seen in chapter 4, the mobilities of all three samples are almost linear in $1/T$ at room temperature. This is consistent with the discussion in chapter 4 that polar optical phonon dominates the electronic scattering at high temperatures.

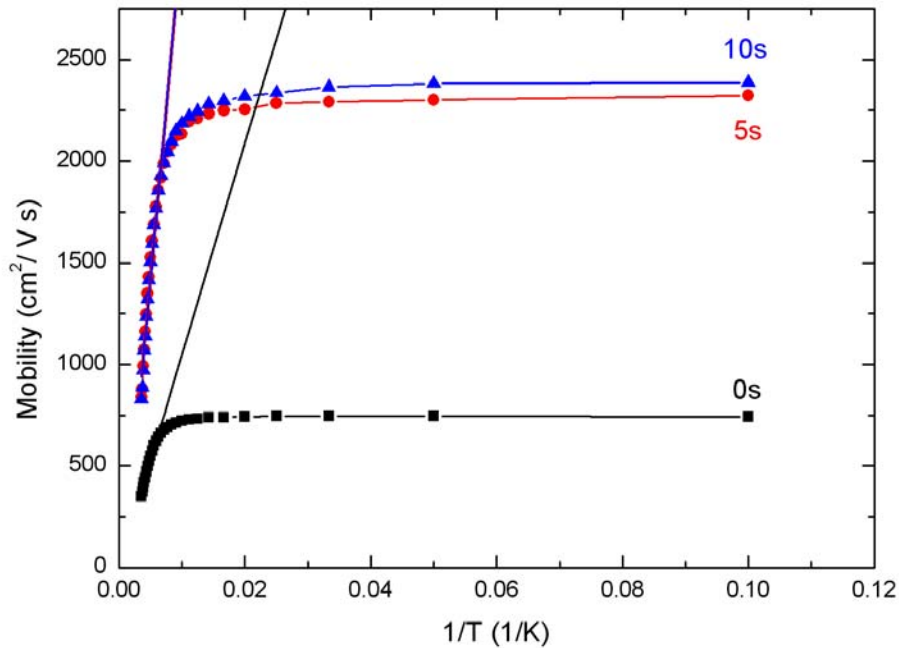


Figure 5-6. Mobility as a function of $1/T$. We can see the linear dependence at room temperature.

5-4 Summary

In this chapter, we have performed measurements on $\text{Al}_{0.15}\text{Ga}_{0.85}\text{N}/\text{GaN}$ HEMTs on silicon substrates over a wide temperature range. Our results indicate that the carrier concentrations, within experimental errors, exhibit little variation from room temperature to low temperatures. This demonstrates the formation of a 2DEG in our system even at room temperature.

In addition, we see that the mobility was greatly enhanced after we deposited Si_3N_4 in the sample. This is consistent with the fact that Si_3N_4 can reduce the stress of GaN on a silicon substrate, and hence we are able to grow high-quality GaN to form a high-mobility 2DEG at the interface of AlGaN and GaN.

Next, we compared the mobility with the results from chapter 4. It shows that $\text{Al}_{0.15}\text{Ga}_{0.85}\text{N}/\text{GaN}$ HEMTs on sapphire substrates has a very high mobility of $6600 \text{ cm}^2/\text{Vs}$. We conclude that it is very difficult to grow

AlGaN/GaN HEMTs on silicon substrates, which have mobilities as high as those grown on sapphire substrates. However, the great enhancement of the mobility demonstrates the usefulness of our technique. With optimization of the growth temperature, HEMT structure, and most importantly, Si₃N₄ treatment technique, it is expected that the quality of HEMTs grown on silicon substrates could be as high as those grown on conventional sapphire substrates. This paves the way for a possible experimental realization of the integration of the GaN/AlGaN HEMTs with the very mature silicon technology in industry.

References

1. Y. F. Wu, B. P. Keller, S. Keller, D. Kalponek, P. Kozodoy, S. P. DenBaas, and U. K. Mishra, *Appl. Phys. Lett.* **69**, 1438 (1996).
2. N. Maeda, T. Saitoh, K. Tsubaki, T. Nishida, and N. Kobayashi, *Jpn. J. Appl. Phys., Part 2* **38**, L799 (1999).
3. T. Egawa, H. Ishikawa, M. Umeno, and T. Jimbo, *Appl. Phys. Lett.* **76**, 121 (2000).
4. S. Nakamura, M. Seno, S. Nagahama, N. Iwasa, T. Yamada, T. Matsushita, Y. Sugimoto, and H. Kiyoku, *Appl. Phys. Lett.* **69**, 4056 (1996).
5. A. Krost and A. Dadgar, *Phys. Stat. Sol. (a)* **194**, 361 (2002).
6. K. Y. Zang, S. J. Chua, L. S. Wang, and C. V. Thompson, *Phys. Stat. Sol. (c)* **0**, 2067 (2003).
7. S. Pal and C. Jacob, *Bull. Mater. Sci.* **27**, 501 (2004).
8. R. Birkhahn and A. J. Steckla, *Appl. Phys. Lett.* **73**, 2143 (1998).
9. H. M. Manasevit, F. M. Erdmann, and W. J. Simpson, *J. Electrochem. Soc.* **118**, 1864 (1971).
10. S. Guha and N. A. Bojarczuk, *Appl. Phys. Lett.* **72**, 415 (1998).
11. S. Guha and N. A. Bojarczuk, *Appl. Phys. Lett.* **73**, 1487 (1998).
12. A. Dadgar, M. Poschenrieder, A. Reiher, J. Bläsing, J. Christen, A. Krtschil, T. Finger, T. Hempel, A. Diez, and A. Krost, *Appl. Phys. Lett.* **82**, 28 (2003).
13. N. C. Chen, C. F. Shih, C. A. Chang, A. P. Chiu, S. D. Teng, and K. S. Liu, *Phys. Stat. Sol. (b)* **241**, 2698 (2004).
14. L. J. Van der Pauw, *Philips Research Report No.* **13**, 1 (1958).
15. Daniel W. Koon, *Rev. Sci. Instrum.* **60**, 271 (1989).
16. Daniel W. Koon, Arshad A. Bahl, and Edward O. Duncan, *Rev. Sci. Instrum.* **60**, 275 (1989).

Chapter 6

Conclusions

As described previously, there exists a two-dimensional electron gas (2DEG) at the AlGa_xN/GaN interface. The 2DEG results from polarization effects, and it can be created at the AlGa_xN/GaN interface of a nominally undoped AlGa_xN/GaN high electron mobility transistor (HEMT). In this thesis, I have reported two measurements on AlGa_xN/GaN HEMTs, and there have been a number of interesting phenomena as outlined below.

In chapter 4, measurements on 3 different Al_xGa_{1-x}N/GaN HEMTs samples with different Al-contents (11%, 15%, and 25% respectively) revealed that the one with 15% Al content has the highest mobility. The GaN was grown on sapphire substrates by metal organic vapor phase epitaxy (MOVPE).

In addition, the measurement on the 2DEG carrier concentration showed that it increases with increasing Al content. Quantitative calculations of the 2DEG concentration by us agree with the observation. The reason for this is that when the Al fraction increases, the polarization in Al_xGa_{1-x}N increases accordingly, and this polarization increment will induce more sheet charges at the interface of Al_xGa_{1-x}N and GaN. Therefore, for an Al_xGa_{1-x}N/GaN heterostructure with a higher Al composition, more electrons would be attracted to compensate for the sheet charges near the Al_xGa_{1-x}N/GaN interface, resulting in a higher 2DEG concentration.

We also measured the activation energy of Al_xGa_{1-x}N/GaN HEMTs, and found out that it increases with increasing Al content. As the Al content increases, the lattice mismatch between Al_xGa_{1-x}N and GaN becomes more prominent. This increased lattice mismatch could induce a larger defect density. Therefore a higher activation energy is required to thermally activate the carriers into the 2DEG region.

Finally, the fact that the Al_xGa_{1-x}N/GaN HEMTs with 15% Al content has the highest mobility suggests that we should keep the Al content at 15% for the greatest mobility in our next study.

In chapter 5, using the result of chapter 4 as our guideline, we set

the Al content at 15% when growing high-mobility AlGaN/GaN HEMTs on Si substrate. Si was chosen as our substrates because it could be combined with the very mature Si technology in industry. However, our result indicated that AlGaN/GaN HEMTs grown on Si substrate did not have high mobility. Hence, we inserted Si₅N₄ thin films with 5 seconds and 10 seconds deposition time after AlN was grown on the Si substrates. The result is that the mobility was greatly enhanced, almost three times larger than that without a Si₅N₄ layer.

Furthermore, in comparison with the results of the previous chapter, we see that Al_{0.15}Ga_{0.85}N/GaN HEMTs on sapphire substrates have much higher mobility (6600 cm²/Vs). We conclude that it is difficult to grow AlGaN/GaN HEMTs on silicon substrates which have mobilities as high as those grown on sapphire substrates. However, this great enhancement of the mobility demonstrates the usefulness of our technique. With optimization of our growth temperature, HEMT structure, and most importantly, Si₅N₄ treatment technique, it is expected that the quality of HEMTs grown on silicon substrates can be as high as those grown on conventional sapphire substrates. This paves the way for a possible experimental realization of the integration of GaN/AlGaN HEMTs with the very mature silicon technology in industry.